

Mesospheric Bore Evolution and Instability Dynamics Observed in PMC Turbo Imaging and Rayleigh Lidar Profiling Over Northeastern Canada on 13 July 2018

David C. Fritts^{1,2} , Natalie Kaifler³ , Bernd Kaifler³ , Christopher Geach⁴, C. Bjorn Kjellstrand⁵ , Bifford P. Williams¹ , Stephen D. Eckermann⁶ , Amber D. Miller⁷, Markus Rapp³ , Glenn Jones⁸, Michele Limon⁹ , Jason Reimuller¹⁰, and Ling Wang¹

¹GATS, Boulder Division, Boulder, CO, USA, ²Center for Space and Atmospheric Research, Embry-Riddle Aeronautical University, Daytona Beach, FL, USA, ³German Aerospace Center (DLR), Munich, Germany, ⁴School of Physics and Astronomy, University of Minnesota, Minneapolis, MN, USA, ⁵Department of Physics, Columbia University, New York, NY, USA, ⁶Space Science Division, U.S. Naval Research Laboratory, Washington DC, USA, ⁷Department of Physics and Astronomy, University of Southern California, Sacramento, CA, USA, ⁸Rigetti Computing, Berkeley, CA, USA, ⁹Department of Physics and Astronomy, University of Pennsylvania, Philadelphia, PA, USA, ¹⁰Integrated Spaceflight Services, Boulder, CO, USA

Key Points:

- Mesospheric bores are dramatic events that dominate local instability dynamics accompanying their passage
- Mesospheric bores can exhibit significant variability in their evolution in time and along their phases
- Mesospheric bores can exhibit significant instability dynamics at smaller spatial scales at their leading and trailing edges

Supporting Information:

- Supporting Information S1
- Figure S1
- Figure S2
- Figure S3
- Figure S4
- Figure S5
- Figure S6
- Figure S7
- Figure S8
- Figure S9
- Figure S10
- Figure S11
- Figure S12
- Movie S1

Correspondence to:

D. C. Fritts,
dave@gats-inc.com

Citation:

Fritts, D. C., Kaifler, N., Kaifler, B., Geach, C., Kjellstrand, C. B., Williams, B. P., et al. (2020). Mesospheric bore evolution and instability dynamics observed in PMC Turbo imaging and Rayleigh Lidar profiling over Northeastern Canada on 13 July 2018. *Journal of Geophysical Research: Atmospheres*, 125, e2019JD032037. <https://doi.org/10.1029/2019JD032037>

Received 12 NOV 2019

Accepted 22 APR 2020

Accepted article online 26 APR 2020

©2020. The Authors.

This is an open access article under the terms of the Creative Commons Attribution-NonCommercial-NoDerivs License, which permits use and distribution in any medium, provided the original work is properly cited, the use is non-commercial and no modifications or adaptations are made.

Abstract Two successive mesospheric bores were observed over northeastern Canada on 13 July 2018 in high-resolution imaging and Rayleigh lidar profiling of polar mesospheric clouds (PMCs) performed aboard the PMC Turbo long-duration balloon experiment. Four wide field-of-view cameras spanning an area of $\sim 75 \times 150$ km at PMC altitudes captured the two evolutions occurring over ~ 2 hr and resolved bore and associated instability features as small as ~ 100 m. The Rayleigh lidar provided PMC backscatter profiling that revealed vertical displacements, evolving brightness distributions, evidence of instability character and depths, and insights into bore formation, ducting, and dissipation. Both bores exhibited variable structure along their phases, suggesting variable gravity wave (GW) source and bore propagation conditions. Both bores also exhibited small-scale instability dynamics at their leading and trailing edges. Those at the leading edges comprised apparent Kelvin-Helmholtz instabilities that were advected downward and rearward beneath the bore descending phases extending into an apparently intensified shear layer. Instabilities at the trailing edges exhibited alignments approximately orthogonal to the bore phases that resembled those seen to accompany GW breaking or intrusions arising in high-resolution modeling of GW instability dynamics. Collectively, PMC Turbo bore imaging and lidar profiling enabled enhanced definition of bore dynamics relative to what has been possible by previous ground-based observations, and a potential to guide new, three-dimensional modeling of bore dynamics. The observed bore evolutions suggest potentially important roles for bores in the deposition of energy and momentum transported into the mesosphere and to higher altitudes by high-frequency GWs achieving large amplitudes.

1. Introduction

Polar mesospheric cloud (PMC) Turbo imaging examined to date has revealed a wide diversity of mesospheric dynamics ranging from instabilities and turbulence at scales as small as ~ 100 m to larger-scale dynamics that extend beyond the $\sim 75 \times 150$ -km projected field of view (FOV) at ~ 82 km (see the PMC Turbo overview by Fritts, Miller, et al., 2019, hereafter F19). Among these dynamics are multiple occurrences of larger-scale apparent gravity wave (GW) breaking and self-acceleration (SA) events, and mesospheric bores. Prolific smaller-scale responses include Kelvin-Helmholtz instabilities (KHI) at a range of scales and other features not yet identified.

Our topic of interest here, mesospheric bores, are examples of nonlinear responses to GW amplification and trapping in ducts. Ducts occur where the background environment yields a finite GW vertical wavelength, λ_z , and $m^2 > 0$ (with $m = 2\pi/\lambda_z$ where m is real) over an altitude range confined between regions in which the GW is evanescent (with $m^2 < 0$) for specified GW horizontal wavelength, λ_h , and environmental fields. In many cases, ducts arise, in part at least, due to strong GW forcing, often accompanying SA dynamics that yield significant local mean-flow accelerations. Ducts comprise either strong inversion layers

Author Contributions:

Conceptualization: David C. Fritts, Amber D. Miller
Formal analysis: David C. Fritts, Natalie Kaifler, Bifford P. Williams
Funding acquisition: David C. Fritts, Stephen D. Eckermann, Markus Rapp
Investigation: David C. Fritts, Natalie Kaifler, Christopher Geach, C. Bjorn Kjellstrand, Bifford P. Williams, Stephen D. Eckermann
Methodology: David C. Fritts, Natalie Kaifler, Bernd Kaifler, Christopher Geach, C. Bjorn Kjellstrand, Bifford P. Williams, Markus Rapp, Glenn Jones, Michele Limon, Jason Reimuller, Ling Wang
Project administration: David C. Fritts
Resources: Stephen D. Eckermann, Amber D. Miller, Markus Rapp
Software: Bernd Kaifler, Christopher Geach, C. Bjorn Kjellstrand, Glenn Jones
Supervision: David C. Fritts
Validation: Bernd Kaifler, Stephen D. Eckermann
Visualization: Natalie Kaifler, Christopher Geach
Writing - original draft: David C. Fritts
Writing - review & editing: Natalie Kaifler

(with localized high atmospheric stability, N^2 , for buoyancy frequency N), local wind maxima along the GW or bore propagation direction, or a combination of the two, referred to as thermal, Doppler, or joint thermal-Doppler (or “dual”) ducts (Chimonas & Hines, 1986; Fritts & Yuan, 1989).

Ducts occur throughout the atmosphere, in the oceans, and have related responses in rivers that have been extensively investigated for over a century (Rayleigh, 1908; Lamb, 1932; Lighthill, 1979, hereafter L79). At lower altitudes, ducts support various nonlinear responses including surface, internal, and undular bores that form, evolve, and ultimately disappear due to the competing influences of dispersion, nonlinearity, instability, and dissipation (see Benjamin, 1967; Davis & Acrivos, 1967; and Grimshaw, 1981a, 1981b, 1981c, 2002; also see Christie, 1989; Rottman & Einaudi, 1993; Rottman & Grimshaw, 2003; and Smith, 1988). More recent observations, modeling, and theory have addressed various bore dynamics in the mesosphere and lower thermosphere (MLT). These studies are reviewed below and provide the context for our analyses presented in this paper.

The initial mesospheric undular bore observations by Swenson and Epsy (1995) and Taylor et al. (1995) reported on “wall” waves that exhibited apparent bore features, but which were previously undocumented in the MLT. These observations spawned significant interest in mesospheric bores by many authors that continues to the present. Motivated by the Taylor et al. (1995) observations, Dewan and Picard (1998, 2001, hereafter DP98 and DP01) suggested that undular bore structure could be described approximately by two-layer shallow-water theory following Rayleigh (1908). The extensive DP98 analysis led to predictions for relations among bore wavelengths, amplitudes, phase speeds, duct depths, and implied temperature perturbations (T'), a number of which were found to be qualitatively correct in multiple applications to subsequent bore observations and analyses. DP98 also estimated the rate at which successive bore crests are added due to dissipation.

DP01 further explored the potential for bore generation via local GW pseudo-momentum deposition (hereafter referred to as momentum deposition, though the momentum always resides in the mean flow) in a thermal duct due to GW critical level interactions. This general hypothesis is supported by the study by Fritts et al. (2018) that demonstrated strong local momentum deposition and a mean wind jet formation for a large-amplitude GW encountering a mesospheric inversion layer (MIL), such as those attributed with supporting bore propagation by DP98 and multiple observational papers discussed below. The jet formation in that study was due to a horizontally periodic GW. However, localized GW momentum deposition and resulting local mean wind accelerations are an obvious candidate for bore generation for a sufficiently large GW amplitude. Related studies by Chimonas et al. (1996), Walterscheid et al. (2001), Snively and Pasko (2003, 2008) and Fritts et al. (2018) demonstrated the potential for GWs impinging on a thermal or emerging Doppler duct to become trapped and exhibit instabilities, secondary GWs (SGWs), and partial transmission and/or reflection thereafter, depending on the duct and GW parameters. However, none of these studies examined the larger-scale responses to localized momentum deposition that might lead to horizontally confined bore generation.

Motivated by multiple early observational studies of bores seen in one or several airglow emissions and the application of two-layer, shallow-water theory to mesospheric bores by DP98, Laughman et al. (2009, hereafter L09) performed a series of numerical simulations of large-amplitude GWs having various λ_h and amplitudes propagating into multiple thermal, Doppler, and dual-ducting environments. L09 results relevant to our current bore study include the following:

- 1 thermal ducts experiencing GW forcing at large λ_h and sufficiently large GW amplitudes yield undular bores having smaller λ_h that increase with time,
- 2 regions below (above) the duct experience rapid increases (decreases) in T and airglow brightness as the bore leading crest passes, and more gradual returns as the remaining bore passes and/or abates,
- 3 deeper thermal ducts allow more complex responses and variability in space and time, likely due to additional modes with smaller λ_z excited, and trapped, in the ducts,
- 4 Doppler ducts allow trailing (and leading) crest formation and λ_h reductions with time,
- 5 dual ducts enable characteristics of each and asymmetric, phase-shifted responses in the vertical, trailing and leading crest formation, and λ_h compression with time.

More recent modeling and theoretical studies compared undular bore evolutions from initial solitary waves and larger-scale GWs in thermal ducts described by the Navier-Stokes equations and the Benjamin-Davis-Acrivos-Ono (BDAO) model (Benjamin, 1967; Grimshaw et al., 2015, hereafter G15; Laughman

et al., 2011, hereafter L11) and their dissipation via GW radiation. L11 compared the N-S and BDAO solutions for various initial conditions and found close agreement in several cases at earlier times. At later times, significant differences arose in the bore phase speed and the rate of trailing crest formation. Specific L11 findings include the following:

- 1 slower undular bore evolutions occur for initial solitary wave and longer initial GW wavelengths and/or smaller amplitudes using the full N-S equations,
- 2 viscosity yields smaller initial undular bore amplitudes, but faster bore propagation,
- 3 large-amplitude initial GWs yield rapid evolutions and expectations for strong bore instabilities that are not captured by the BDAO solutions, and
- 4 both the Navier-Stokes and BDAO solutions yield generation of trailing crests having λ_n that increase with time for thermal ducts (in contrast to the Doppler ducts in L09).

Both L11 and G15 examined the influences of nonzero background stability outside a thermal duct on undular bore evolutions, as this is expected to be a factor in virtually all cases. Results of these studies include the following:

- 1 nonzero external stability enables radiated GWs that remove energy from ducted responses and slow undular bore evolutions,
- 2 energy removal by GW radiation contributes to bore dissipation, but on time scales that are sufficiently long to enable their detection, and
- 3 N-S and revised BDAO solutions accounting for external stratification yield reasonable agreement for bore characteristics and GW radiation contributing to their dissipation.

Mesospheric bore observations prior, and subsequent, to these theoretical and modeling studies confirmed many predictions of bore behavior under various conditions. Multiple studies employing two or more airglow emissions provided evidence of the rapid increases (decreases) in T and airglow brightness below (above) as the bore leading crest passes, confirming the initial observations by Taylor et al. (1995) and the theoretical and modeling studies by DP98 and L09 (Brown et al., 2004; Smith et al., 2003, 2005; Walterscheid et al. 2012). Many additional studies employed ground-based airglow or PMC imagers, lidars, radars, and/or satellite T profiles to infer the character (thermal, Doppler, or dual) of the ducts supporting bore propagation, potential sources (Brown et al., 2004; Giongo et al., 2018; Smith et al., 2003, 2005, 2017; Yue et al., 2010), and other aspects of the generation, evolution, and dissipation (Bageston et al., 2011; Bageston et al., 2011; Batista et al., 2002; Brown et al., 2004; Dalin et al., 2013; Fehine et al., 2005; Fehine et al., 2009a; Fehine et al., 2009b; Li et al., 2007, 2013; Medeiros et al., 2001, 2005, 2016, 2018; Narayanan et al., 2009, 2012; Nielsen et al., 2006; She et al., 2004; Shiokawa et al., 2006; Smith, 2014; Smith et al., 2003, 2005, 2006, 2017; Stockwell et al., 2006, 2011; Yue et al., 2010). Interesting aspects of the initial “wall” wave included enhanced T and Na column density (Swenson et al., 1998). Li et al. (2013) provided a particularly comprehensive review of the observational bore studies to that time. Significantly, however, some implications of modeling have been challenging to evaluate for lack of sufficient resolution in earlier imaging studies, and modeling has yet to address more realistic bore forcing and the consequences for instability character and momentum deposition in representative environments.

Despite suggestions and evidence of bore forcing by large-amplitude GWs in environments having, or enabling formation of, suitable ducts, however, neither weakly nonlinear theory nor nonlinear modeling to date has examined potential bore forcing by localized high-frequency GW packets approaching breaking amplitudes. Increasing observations of mesospheric bores, as their diverse characteristics become more widely appreciated and recognized, suggest that they may play more significant roles in atmospheric dynamics and structure than previously believed. Specifically, we expect that they make significant contributions to deposition of momentum transported into the MLT by GWs generated at lower altitudes. As an example, GW momentum deposition accompanying GW breaking is assumed to occur over extended altitudes in most GW parameterizations, which impose slowly varying GW amplitudes consistent with overturning in “Lindzen”-like schemes. But if bores—or local bore-like responses—play major roles in GW dissipation because they often arise in what we know to be highly structured environments (inertia-GWs and tides dominate the velocity and wind shear variances at all altitudes below ~ 125 km), then GW momentum deposition will likely also be highly structured in altitude and localized horizontally. If so, such momentum deposition will be partitioned among local mean-flow accelerations and SGWs that will have scales

determined by the spatial and temporal scales of the local forcing, with likely different implications for mean forcing than current parameterizations.

Several bore features that are of interest in this study were addressed previously to varying degrees. These include ducting character (Bageston, Wrasse, Batista, et al., 2011; Bageston, Wrasse, Hibbins, et al., 2011; Fechine et al., 2009b; Smith et al., 2003; She et al., 2004; Stockwell et al., 2011), successive bores at an evolving duct (Medeiros et al., 2016; Smith et al., 2017), and evidence of instabilities accompanying bore evolution and dissipation (Medeiros et al., 2018; She et al., 2004; Smith et al., 2005; Stockwell et al., 2011; Yue et al., 2010). PMC Turbo measurements offer a new perspective on these bore dynamics because they reveal bore structures, evolutions, and displacements at high resolution in horizontal imaging and vertical profiling. A major additional benefit is the ability to describe instabilities accompanying bore formation and dissipation, which, to our knowledge, has not been possible in previous studies. As a result, PMC Turbo observations provide new analysis capabilities and insights into these dynamics when they exhibit responses at the PMC layer.

Our paper is organized as follows. Section 2 briefly describes the PMC Turbo experiment imaging and lidar profiling systems. An overview of the two bore events is provided in section 3. Detailed analyses of the two bore evolutions, structures, and associated instabilities are presented in sections 4 and 5. These analyses demonstrate the benefits of combined imaging and profiling in quantifying bore and related instability dynamics. Section 6 discusses these results in relation to previous bore and instability studies and the implications for the bore ducting environments. A summary and our conclusions are provided in section 7.

2. PMC Turbo Instrumentation

PMC Turbo flew on a NASA long-duration balloon from Erange, Sweden to northeastern Canada for ~5.5 days at an altitude of ~38 km in July 2018 (see F19a, for an overview and examples of the observations). Of relevance to this paper, PMC Turbo instruments included four large field-of-view (FOV) imagers aligned to provide a composite image having a projection at the measured PMC altitude of ~82 km of ~75 × 150 km in the antisun direction and the Balloon Lidar Experiment (BOLIDE) Rayleigh lidar providing near-vertical profiling at the near-zenith edge of the composite imaging FOV.

PMC imaging employed in this study used 4 × 4 pixel binning to increase the signal-to-noise, due to often relatively weak PMC brightness over much of the composite FOV along the PMC Turbo flight track between 65° and 70°N. This resulted in horizontal resolution of ~50 m, which proved sufficient to resolve many small-scale features not previously identified in the PMC layer. Our analysis below employed both projected, composite wide FOV imaging, and individual wide FOV camera unprojected imaging for our various analysis components.

The BOLIDE 4.6-W laser operated at 532 nm, employed a 100-Hz pulse repetition frequency, and was pointed 28° off-zenith within the near zenith edges of the central large FOV cameras. Backscattered photons were detected using a 0.5-m diameter telescope and three height-cascaded receiving channels behind 0.3 nm wide filters. Raw photon count data can be variably binned depending on available signal-to-noise ratio (SNR) and required resolution. Here, we used 60-m vertical and 30-s temporal resolution and 20-m vertical and 10-s temporal resolution, depending on the event character being analyzed. Background photon counts were subtracted from photon count profiles by a fitted linear function between 96 and 135 km altitude. Range was corrected taking the off-zenith pointing into account. The PMC backscatter ratio was obtained by normalization to the MSIS-E-90 density profile between 60- and 75-km altitudes and converted to a volume backscatter coefficient β following Thayer and Nielsen (1995). For each profile, the variance between 88- and 90-km altitudes was used to determine significant PMC backscatter at 3σ . Additionally, T and T' were obtained using hydrostatic integration of the backscatter profiles (Kaifler et al., 2015) with an initial mean T obtained from the Microwave Limb Sounder aboard the Aura satellite below the PMC layer (also see caveats below).

3. Two Bore Event Overview

In order to relate our PMC Turbo bore observations to previous studies, a distinction needs to be made between bore responses seen in PMC brightness and airglow imaging, the latter of which was employed

to define bore evolutions in the horizontal plane in the majority of previous studies. Airglow brightness perturbations correlate with T' and provide evidence of vertical displacements above and below the bore duct accompanying bore passage, but less clear responses at the bore duct. PMC brightness variations, especially gradients, track the advection of individual air parcels spanning the PMC layer, especially where PMC particle brightness does not change rapidly on short timescales. Where this assumption is valid, vertically integrated PMC brightness variations are largely indicative of horizontal convergence and divergence. Where vertical excursions are large and downward; however, they drive large increases in T , and significant sublimation can occur on short timescales and result in significantly reduced integrated brightness for 10's of min or longer thereafter at the lowest altitudes (see the discussion accompanying Figure 2 below).

Two successive apparent bores (hereafter Bore 1 and 2) were observed in PMC Turbo imaging and BOLIDE measurements southwest of Franklin Lake in Nunavut, Canada on 13 July 2018. In the local morning hours between 12 and 14 UT, the gondola was floating largely westward from 66.3°N, 94.9°W toward 66.5°N, 97.6°W at 12 ± 3 m/s and a 39.3 ± 0.2 -km altitude. Antisun pointing of the gondola, and thus the central viewing of the PMC wide-FOV composite imaging and BOLIDE profiling, rotated from 256° to 282° clockwise from north during this time and thus were viewing largely toward west in the direction of gondola drift. The bore evolutions are shown in projected FOV imaging and PMC profiling in Figures 1 and 2. A movie of the bore evolutions in a 4-camera projected FOV (Data S1 in the supporting information) is provided as supplemental materials.

Referring to Figure 1, we see that Bore 1 exhibited one initial bright phase, but evolved three additional leading phases and a clear trailing phase prior to abating, suggesting an undular bore character throughout its evolution. It entered the Camera 4 FOV from the south at ~12 UT, propagated slightly W of N, and exhibited significant phase and λ_h variations throughout its evolution (see Figure 1 from 12:15–13:05 UT and the more detailed discussion of Bore 1 dynamics and evolution in section 4 below). A significant feature that will also be discussed extensively below was seen from ~12:25–12:35 UT and provided evidence of initial Bore 1 forcing by localized GW SA dynamics. A successive leading phase and a trailing phase arose quickly, and two additional leading phases arose thereafter. All phases exhibited instabilities contributing to Bore 1 dissipation throughout its evolution. A further aligned, transient, but apparently unrelated single phase arose at ~13:00 UT, became strong by ~13:10 UT, but broke up quickly thereafter (see Data S1).

Bore 2 seen emerging at 13:25 UT in Figure 1 exhibited very different character, compressed horizontally and intensified initially to a single bright phase, suggesting an initial solitary wave response. Thereafter, it separated into multiple, smaller-scale phases at more westward locations, suggesting a transition to an apparent undular bore at more western locations along its initial phase. Like Bore 1, Bore 2 also exhibited instabilities and apparent dissipation throughout its evolution.

Both bores occurred during a PMC layer descending from ~84 to ~80 km from ~09–13:30 UT, with deeper, transient descents accompanying the major Bore 1 and 2 phases at ~12:34 and 13:34 UT (Figures 2a and 2b). Peak PMC brightness increased somewhat at ~10:40 UT and more significantly beyond ~12:10 UT approaching the downward displacement labeled Phase 2 in Figure 2b. PMC brightness decreased sharply accompanying the rapid descent and implied strong adiabatic warming over ~4 min of the feature labeled Phase 2. PMC brightness increased again after ~13:15 UT approaching the feature labeled Bore 2, and again decreased sharply accompanying its rapid descent for the same reason.

Descending features preceded both bores at observed periods of ~9 and 15–17 min, respectively. Those leading Bore 1 at the Bolide measurement location at these times (see the red dots at right in the second and third panels of Figure 1) revealed likely small-scale GWs that exhibited weak brightness variations and ambiguous phase orientations at 12:15 UT. These hinted of an E-W phase alignment at 12:25 UT, suggesting a possible emerging Bore 1 leading phase ahead of the brighter and more distinct successive phases having similar alignments to the south. No clear phase structure was seen ahead of the single bright feature emerging from 12:25–12:35 UT identified as Bore 2.

The large-scale descent of the bright PMC layer beginning ~11:30 UT ahead of Bore 1, and the vertical divergence of the full PMC layer beginning at ~12:10 UT suggested horizontal convergence at a central altitude that contained the duct along which Bore 1 propagated. A similar morphology was suggested by the behavior at the PMC layer beginning ~12:55 UT ahead of Bore 2, but in this case, the Bore 2 response appeared to have been deeper, and the upper features were not revealed by PMC profiling. These features are consistent with

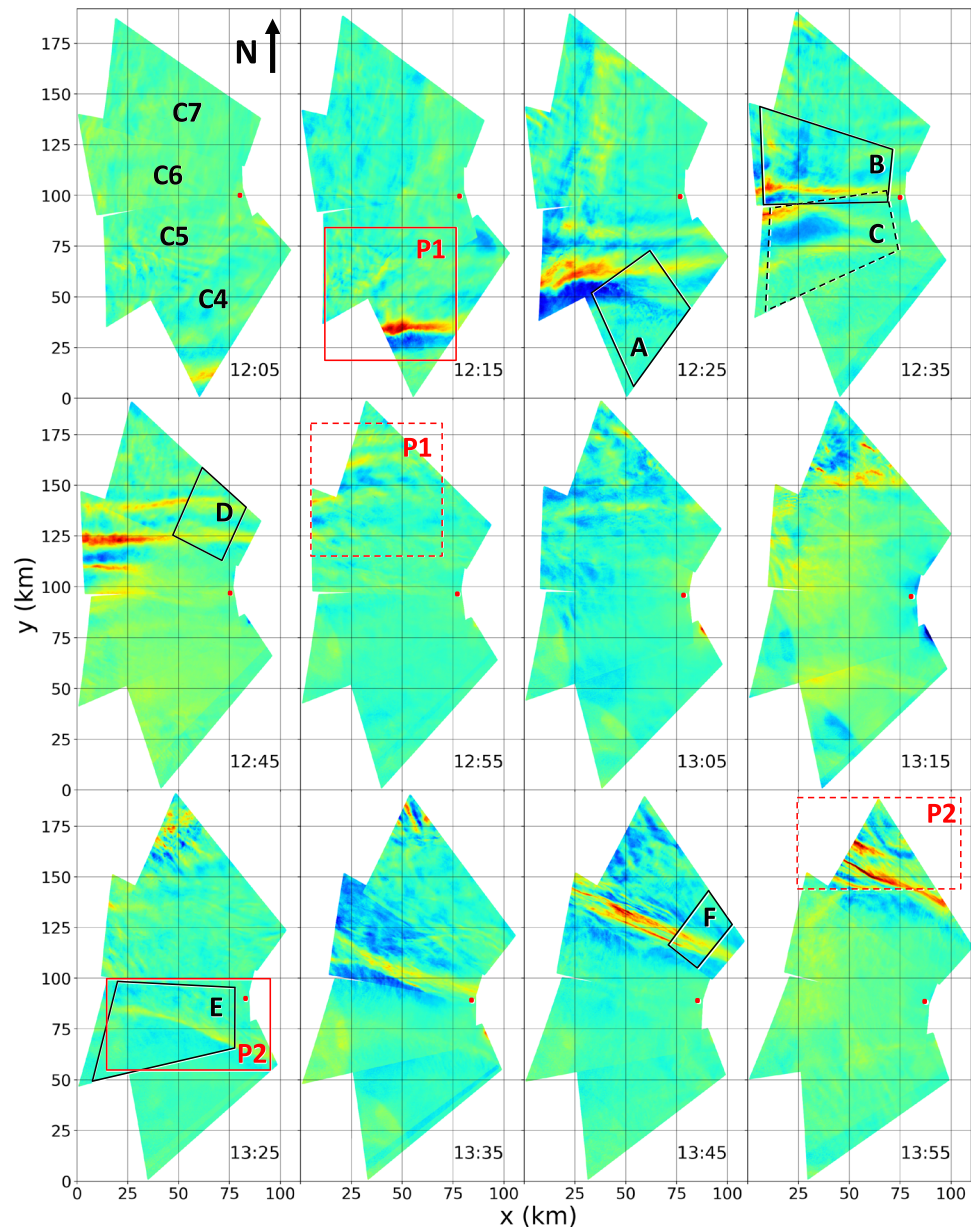


Figure 1. Composite PMC wide-FOV imaging projected to 82 km spanning the two bore events at a 10-min cadence. The color scale varies from very weak PMC brightness (dark blue) to high PMC brightness (dark red). The lidar viewing location at ~82 km is shown with a red dot at center right in each panel; Cameras 4–7 are labeled at top left. Rectangles (quadrangles) show regions, and intervals for which projected (unprojected) images are shown in subsequent figures.

expectations of bore theory and modeling, and with inferences from previous studies employing airglow imaging. Additional descending features following Bore 2 at ~14:00 and 14:40 UT suggested other similar, but weaker, responses that may have exhibited similar character at a persisting duct.

The decrease in brightness following passage of Bore 1 Phase 2 was too rapid to be explained by horizontal divergence, however. Instead, the most likely cause was decreasing PMC particle size and brightness due to sublimation approaching, and at, the lowest altitudes. We expect a mean $T \sim 160$ K at 80 km, based on the mean at ALOMAR at a comparable latitude (Rapp et al., 2004) and a 30 nm particle lifetime at 160 K of only ~4 min (Gadsden & Schröder, 1989; Hervig et al., 2009; Rapp & Thomas, 2006). We also expect a lifetime of ~50 min or longer at 82 km for a mean $T \sim 150$ K based on the same analyses. The implication of varying T for

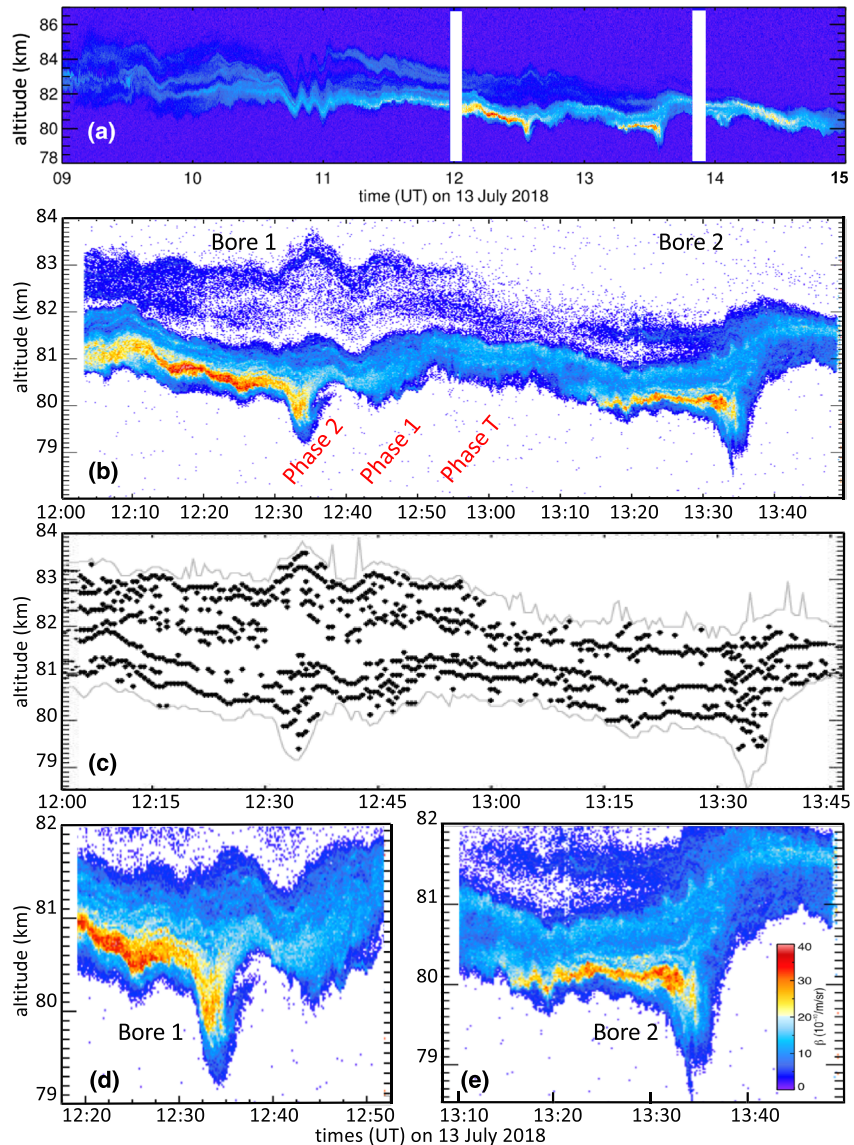


Figure 2. BOLIDE PMC profiling showing (a) the PMC layer evolution from 9–15 UT at 10-s and 60-m resolution, (b) a zoomed section showing the two bores (30-s and 60-m resolution), (c) tracking of individual PMC maxima defining layer motions in the vertical, and (d and e) further zoomed sections showing the fine details of Bores 1 and 2 revealing apparent KHI at the bore lower edges (10-s and 20-m resolution). Note the Bore 1 phases in 2b and the descending tendrils at ~30 s intervals at the lowest excursions of the two bores in d and e. The color scale is shown in panel e.

our purposes is that PMC brightness can serve as a useful tracer of dynamics for these bores, given that the major features of interest are at higher altitudes (above ~80 km) or make only brief excursions to lower altitudes.

BOLIDE profiling also provided evidence of GWs potentially contributing to bore forcing below PMC altitudes. The Rayleigh lidar profiling at altitudes from ~51–80 km enabled estimates of T and T' that revealed likely GW influences from below (see Figure 3 at the earlier times). These data suggest a GW with descending phases at an observed period of ~3 hr and $\lambda_z \sim 17$ km that appeared to undergo breaking above ~65–70 km, potential higher-frequency GWs having larger amplitudes at higher altitudes, and a GW with ascending phases at an observed period >12 hr and $\lambda_z \sim 15$ km that was likely propagating roughly eastward and downshifted in frequency and which may have influenced smaller-scale GW propagation and tendencies for instabilities at various altitudes.

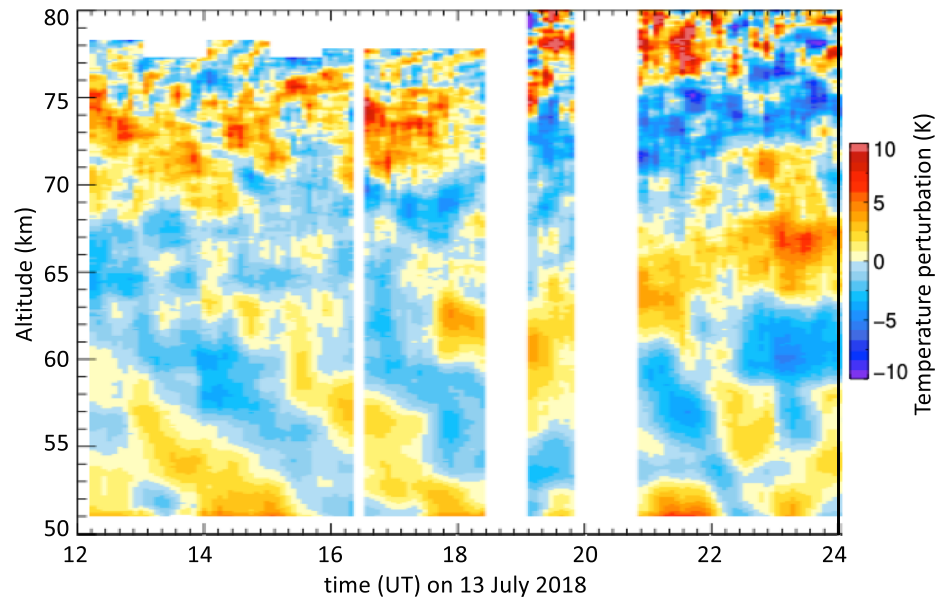


Figure 3. $T'(z,t)$ for 12–24 UT on 13 July showing GWs potentially influencing the bore dynamics from below.

4. Bore 1 Analysis

4.1. Bore 1 Imaging

The Bore 1 evolution in the composite FOV revealed a number of notable features, many of which have not been documented previously. Seen clearly in Figure 1, in zoomed subsets of the composite FOV imaging in Figure 4, and in Data S1 is evidence of local SA dynamics at three successive E-W locations extending eastward from the western edge with time in the composite FOV accompanying a GW propagating toward slightly W of N. See the regions bowed toward N (top) in the initial bright Phase 1 at the earliest times and the accompanying dark regions to the south. SA dynamics yielded advancing GW phases where the GW had the largest amplitude and induced mean motions along its propagation direction (see Fritts et al., 2020). This forcing was apparently influenced by a GW having $\lambda_h \sim 30$ km propagating toward WNW and accounting for the enhanced bright inclined phases seen at lower left in Figure 4 from $\sim 12:17:30$ – $12:30$ UT and which was more evident from $\sim 12:20$ – $12:30$ UT further N. A second region of apparent SA is seen to have emerged north of Phase 1 at $12:27:30$ UT and to have distorted Phase 2 and enhanced brightness contrast until $\sim 12:45$ UT or later. A third region less pronounced than the first and second was seen further east (near the image centers) behind Phase 1 from $\sim 12:27:30$ – $12:42:30$ UT. These SA dynamics suggest that Bore 1 arose due to strong local GW forcing by a primary GW having $\lambda_h \sim 12$ – 14 km at these altitudes and times that propagated largely northward over the interval of apparent Bore 1 forcing.

Importantly, these dynamics were much stronger in the western portion of the composite FOV, implying that the responses seen in PMC profiling at the eastern edge were ~ 2 and 3 times smaller, based on PMC brightness variations along the Bore 1 phases.

Additional evidence for such Bore 1 forcing was provided by PMC imaging revealing strong GW instability dynamics behind and above Phase 1 and a trailing Phase T. Both phases, as they arose, exhibited small-scale trailing structures with roughly normal alignments that evolved to three-dimensional (3-D) structures thereafter (specifically vortex rings oriented roughly horizontally arising from GW breaking; see Figures 4 and 6 at left, also Fritts et al., 2009, 2017). Importantly, the horizontal scales and instability dynamics demonstrate that these smaller-scale GWs necessarily had large momentum fluxes and divergence that implied strong, local forcing of the evolving Bore 1 at its formation stage. The instability dynamics are explored in greater detail in section 4.3 below.

The evolution and progression of Bore 1 phases are further quantified with N-S brightness traces moving with the westward bore advection speed in Figure 5a. Each trace was averaged over 12 km along the bore

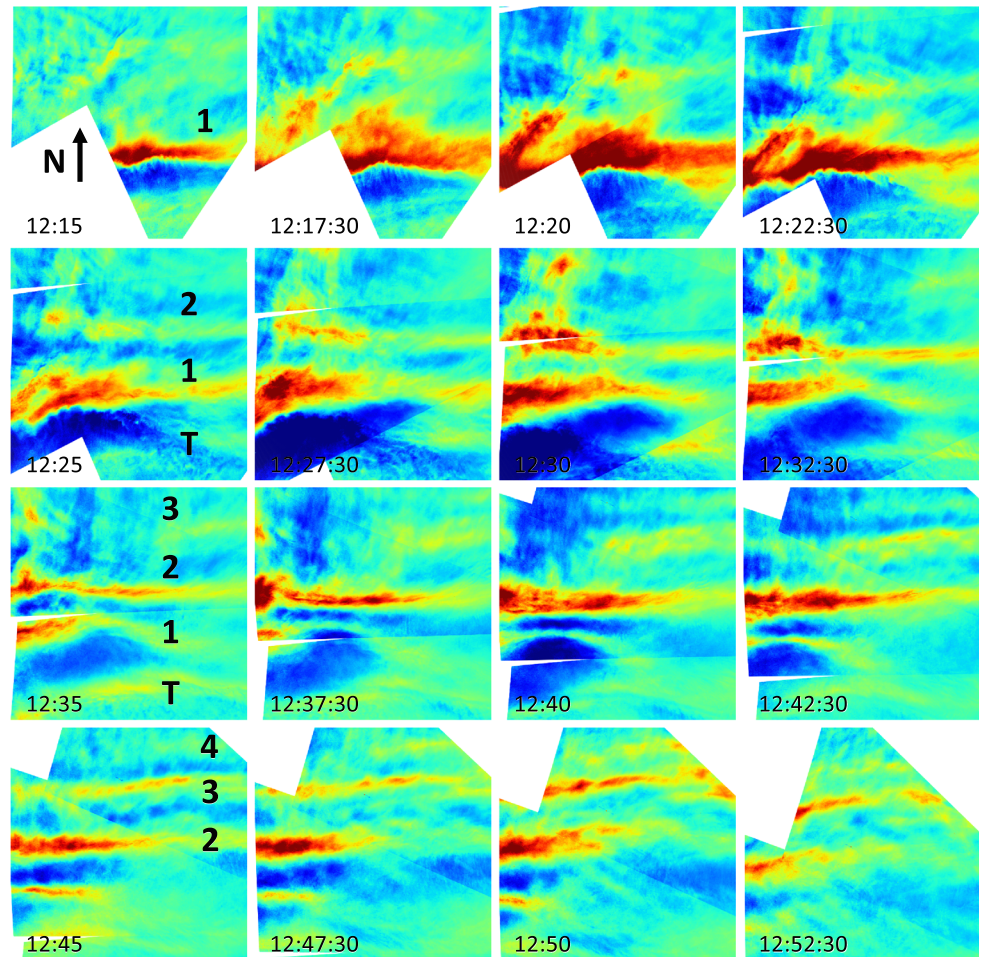


Figure 4. 65×65 km subsections of the composite FOV imaging in region P1 in Figure 1 showing the Bore 1 evolution and propagation at higher spatial and temporal resolution of 2.5 min. Successive phases are labeled as they emerge. The color scale is as in Figure 1.

phases to suppress small-scale features not related to Bore 1, and the mean was removed to more easily identify the locations of brightness maxima.

Subsequent to the apparent Bore 1 forcing, successive phases formed ahead (to the north) of the initial bright phase. The second to form (denoted Phase 2) seen emerging by $\sim 12:20$ UT in Figures 1 and 4 had an initial $\lambda_h \sim 26$ km relative to Phase 1 (also see Figure 5a). This λ_h is consistent with the GW period inferred from PMC profiling discussed at the end of section 3, given the apparent initial Phase 1 phase speed of 55 ± 5 m/s inferred from PMC imaging.

Evidence of an emerging Phase 2 was seen at $\sim 12:20$ UT leading Phase 1 with an apparent Phase 1 and 2 λ_h that decreased from ~ 26 to ~ 15 km from 12:20–12:35 UT (Figures 4 and 5a). Phase 2 exhibited a final observed phase speed of $\sim 44 \pm 5$ m/s thereafter (see Figure 5a). Phase 3 arose at $\sim 12:32:30$ UT ~ 22 km ahead of Phase 2, and a much weaker Phase 4 was first seen clearly at upper right in Figure 4 and in Figure 5a at 12:35 UT ~ 17 km ahead of Phase 3. Phases 3 and 4 exhibited rapid brightening, initial $\lambda_h \sim 21$ and 15 km ahead of the preceding phases, smaller λ_h decreases than for Phase 2, and attainment of final observed phase speeds that appear to agree with that for Phase 2 at later times (see Figure 5a). In contrast, Phase Tarose quickly accompanying initial strong forcing, lagged Phase 1 by ~ 14 km, had a phase speed comparable to Phase 1, but persisted for only ~ 15 min. Additionally, weaker trailing phases emerged beginning $\sim 12:35$ UT and extended further behind the remaining leading phases thereafter, likely accompanying Bore 1 dissipation.

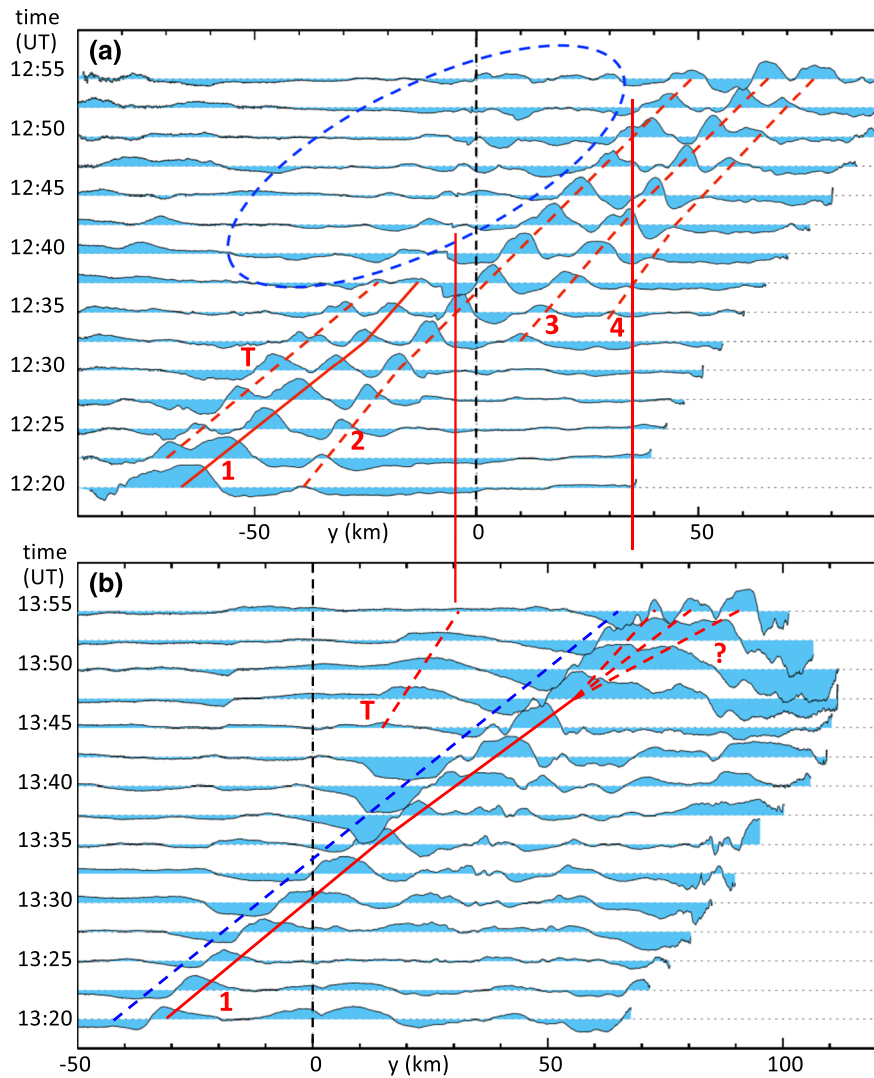


Figure 5. (a and b) PMC brightness perturbations for Bore 1 and 2 at a 2.5-min cadence spanning each event. Solid red lines show apparent primary phase propagation, dashed red lines show secondary leading and trailing phases, the blue oval at top indicates the region of Bore 1 trailing phase dissipation, and the dashed blue line at bottom shows the persistent trailing dark phase of Bore 2.

4.2. Bore 1 BOLIDE Profiling

PMC profiling shown in Figure 2 was seen above to provide insights into the Bore 1 larger-scale GW environment, including the systematic descent of the PMC layer and the larger-scale GWs that appeared to contribute to Bore 1 generation. Figures 2b–2d provide enhanced definition of its structure, evolution, and departures from symmetry at the upper and lower edges of the PMC layer. As noted above, these data also provide insights into the character and evolution of smaller-scale features of Bore 1 behavior. As an example, additional asymmetries are suggested by Figure 2c, which shows local PMC brightness maxima at intermediate altitudes throughout the evolution. These reveal that vertical displacements exhibit a consistent phase structure from ~80.5–82.5 km at ~12:35–12:50 UT. This differs from antisymmetric displacements away from an idealized thermal duct above and below and is suggestive of different bore ducting character to be explored more fully below. These layers also reveal quite weak small-scale motions between the two bores. The most prominent Bore 1 feature in Figure 2 was the sharp descent as the Phase 2 brightness peak passed through the lidar beam. This drop was ~1 km over 4 min (and ~14 km horizontally) and implied an adiabatic warming that impacted total PMC backscatter as described above.

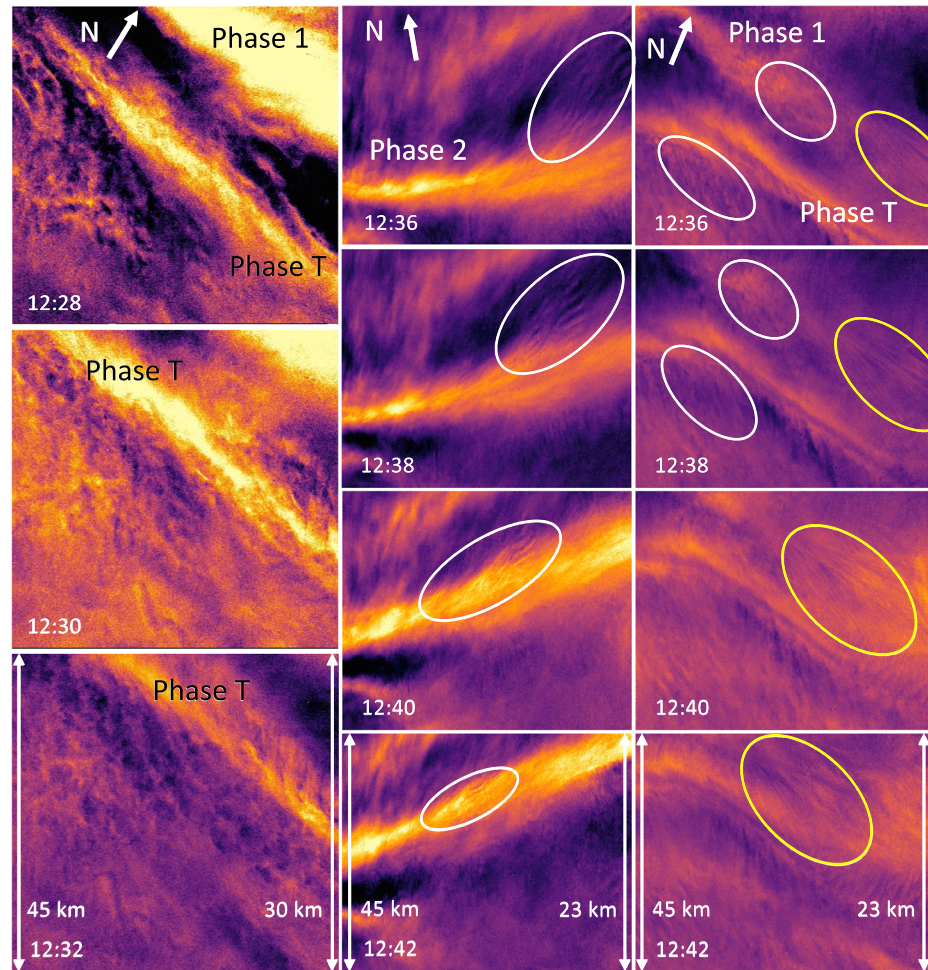


Figure 6. (left) Camera 4 images of vortex rings trailing Phase 1 during SA dynamics; (center) Camera 6 images of KHI entrainment by Phase 2 and trailing instabilities below the bright phase; (right) Camera 5 images during Phase 1 dissipation showing similar features (see regions A, B, and C in Figure 1). The color scale varies from low to high PMC brightness (dark purple to gold/yellow). White ovals in the center column highlight the entraining KHI. Image widths at smaller (larger) zenith angles are shown at right (left) in the last panel of each sequence. White and yellow ovals highlight the smaller-scale instability features discussed in the text.

PMC profiling shown in Figures 2a and 2b from 12–13 UT also revealed that the brightest portion of the PMC layer yielded the largest brightness gradients with increasing altitude at the lower edge of the Bore 1 response. This was fortuitous for our purposes because it enabled tracking of small-scale features that yielded insights into the bore motions accounting for PMC advection and dissipation where bore-induced velocities and shears were likely largest. Variations in PMC brightness spanning the Bore 1 interval in Figures 2b and 2d also indicate strong spatial variations across each Bore 1 bright phase. These imply horizontal convergence and divergence at the PMC layer arising from the Bore 1 phases and potentially GW contributions to Bore 1 forcing or modulation at larger scales (see further discussion below).

Finally, Rayleigh lidar profiling of T' in Figure 3 revealed smaller and larger GW scales and observed periods that may have played roles in defining or modulating Bore 1 forcing and/or the environment in which it arose. Only the smaller periodicities seen at top at earlier times suggest direct GW influences on Bore 1 forcing, but the apparent ascending GW warm phases above ~76 km suggest possible Doppler shifting or downward GW radiation by the bore dynamics.

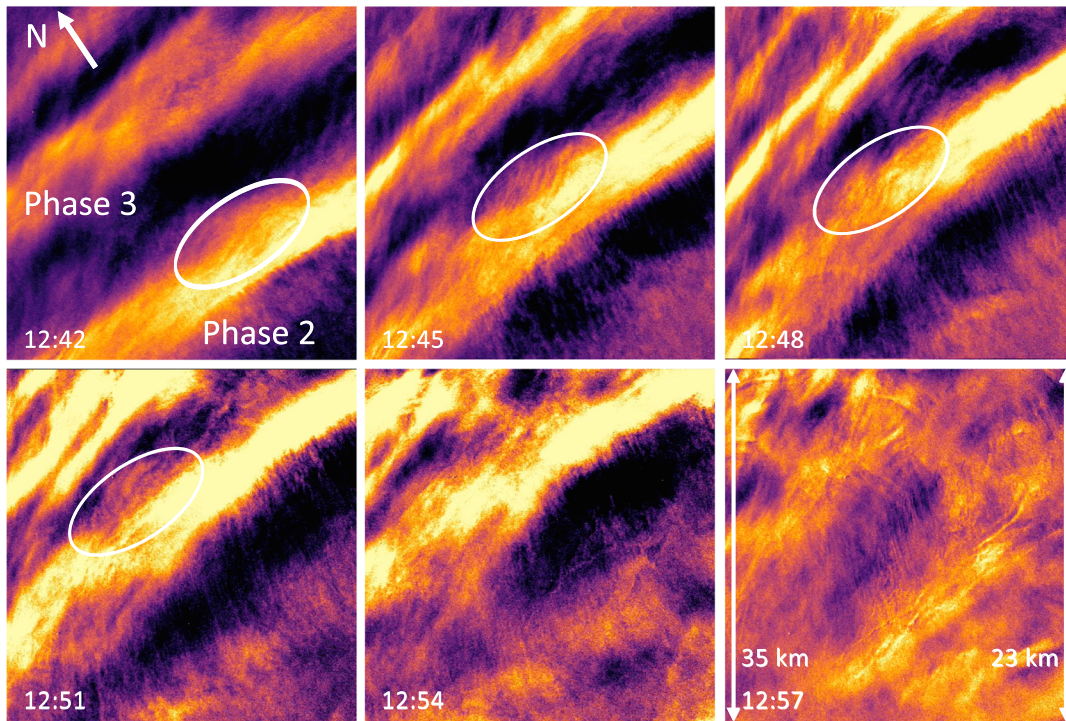


Figure 7. As in Figure 6 showing Bore 1 Phases 2 and 3 dissipation dynamics seen in Camera 7, region D. See text for details.

4.3. Bore 1 Instability Dynamics

Bore 1 exhibited small-scale instabilities at multiple locations throughout its evolution. As noted in section 4.1, instabilities accompanied the GW SA dynamics attributed with Bore 1 generation at the formation stage and thereafter. These instabilities exhibited various forms and evolutions that depended to a significant degree on whether the specific GW/bore phase had attained a large amplitude or was decaying. Strong SA dynamics attributed above with Bore 1 forcing imply GW breaking via vortex ring formation, and this is supported for Bore 1 Phases 1 and T imaging in Figure 4 from 12:20–12:35 UT (see the cusp-like features below these phases), and trailing Phase 1 and especially Phase T in portions of unprojected Camera 4 images from 12:28–12:32 UT at left in Figure 6 (compare the cusp-like features with those described by Fritts et al., 2019). Note the different color scale used to provide greater sensitivity to finer-scale instability dynamics.

The images in Figure 6 at left reveal portions of inclined vortex rings having diameters as large as 5–7 km (sometimes larger) ahead of, between, and behind Phases 1 and T at the earlier times of strong forcing. Based on high-resolution modeling and previous applications to observations of GW breaking, the vortex ring diameters indicate a GW having a minimum $\lambda_z \sim 12\text{--}20$ km and vertical displacements of $\delta z \sim 2$ and 3 km or larger prior to breaking (Fritts et al., 2009). The very close spacing of the vortex rings also implies a high GW intrinsic frequency (see Fritts, Wang, et al., 2019, Figure 7), a potentially larger λ_z , and strong momentum deposition at the central bore altitude that may have contributed to the Bore 1 ducting environment (see further discussion in section 6). Importantly, we should not expect to see evidence of a GW breaking amplitude revealed by vertical displacements, $\delta z \sim \lambda_z/2\pi$, in these regions because GW instabilities will have already reduced GW amplitudes and δz by a factor of ~ 3 or greater (Fritts et al., 2009, 2017).

Referring to Figures 2b and 2d, Figure 4, and the left column of Figure 6, we infer that the vortex rings and associated GW SA dynamics attributed with Bore 1 forcing must have occurred significantly above the deepest Phase 1 descent revealed by PMC profiling of Bore 1. This is because of the dramatically larger variations in brightness (implying a much larger range of vertical excursions and induced T') at the western edges of Cameras 4 and 5 compared to the $\sim 1\text{-km}$ altitude differences at the location of PMC profiling $\sim 60\text{--}80$ km to the east at this same time.

The image sequence in the center column of Figure 6 shows the evolution of Phase 2 and its associated instabilities in unprojected Camera 6 FOVs from 12:36–12:42 UT as Phase 2 intensified, immediately after it passed through the PMC Turbo lidar beam. These reveal entrainment and intensification of initially weak KHI having $\lambda_x \sim 1$ and 2 km beneath and ahead of Phase 2 as it progressed northward (see the small-scale features in the white ovals). We recognize these features as KHI because they exhibit phase variations, evolutions, and secondary instabilities similar to those seen in previous high-resolution imaging, among them Baumgarten & Fritts (2014, hereafter BF14), the latter using PMC Turbo data. These are the features that passed beneath Phase 2 as it was profiled by the lidar. Importantly, while small regions of KHI are seen at multiple locations throughout these bore events, they are not widespread, but reveal regions attaining $Ri < 1/4$ where local shears are conducive. In this case, they arose and intensified approaching Phase 2, implying a localized shear layer depth $\delta z \sim \lambda_x/2\pi \sim 200\text{--}300$ m at onset.

As the KHI passed beneath Phase 2, the shear layer was necessarily driven downward, compressed, and intensified, yielding a further decreasing Ri and causing further KHI intensification and secondary KH instabilities. The bright tendrils extending downward at the deepest descent of Phase 2 revealed in the PMC profiling at these times (see Figure 2d) are direct evidence of the minimum depths and rotation of the KH billows at this phase in their evolution. Specifically, their observed depths were as large as $\sim 300\text{--}500$ m, and these may be significant underestimates, given the influences of deep descents on PMC particle lifetimes discussed above. It is also likely that these Phase 2 dynamics and excursions to lower altitudes were significantly more intense $\sim 40\text{--}80$ km further to the W, given that both the initial forcing and the largest Phase 2 responses thereafter were in that region (see Figure 4 from $\sim 12:25\text{--}12:35$ UT).

The large-scale field in these images advected from right to left (toward W) because of the significant mean westward motions, and the KHI scales appear to compress somewhat because the camera FOV expanded in width at larger off-zenith angles (toward W). The KHI also evolved secondary KHI that only arise for strong primary KHI having a low to intermediate initial Richardson number, $Ri = N^2/(dV/dz)^2 = N^2h^2/V_0^2$, and a high Reynolds number, $Re = V_0h/\nu$, for buoyancy frequency, N , shear layer half depth and half velocity scale, h and V_0 , and kinematic viscosity, ν (Fritts et al., 2014). Secondary KHI manifest as very fine, nearly linear brightness variations aligned largely along the primary KHI, and they contribute to breakdown to turbulence thereafter based on laboratory and modeling studies of these dynamics (also see the discussion in section 6 below of why these can only be KHI). The KHI also yielded evidence of emerging internal convective instabilities (observed and inferred from extensive previous observations, modeling, and theory; see Fritts et al., 2014, and references therein). Together, the secondary KHI and convective instabilities led to the breakup and disappearance of the initial KHI before advecting into the Phase 2 ascending phase (see the last two images in column 2 of Figure 6). These small-scale KHI dynamics motivate several questions regarding their relationship to more general bore dynamics that will be addressed in section 6.

Seen behind Phase 2 (below the bright phase in Figure 6, center column) were small-scale trailing features aligned roughly orthogonal to Phase 2 in several regions and suggesting small-scale transitions to 3-D structures in others. The former closely resemble those observed in the initial high-resolution PMC imaging and modeling comparisons described by Miller et al. (2015). These were due to GW breaking and an event interpreted as an intrusion, both of which evolved to small-scale vortex rings thereafter. Those trailing Phase 2 in Figure 6 exhibiting emerging 3-D structures are seen beginning at the eastern edge of the image initially and progressing westward with time.

As discussed above, Phases 1 and T evolved rapidly and exhibited strong instabilities comprising large-scale vortex rings accompanying Bore 1 forcing by GW SA dynamics in the western portion of the composite FOV. These dynamics subsided as Phase 2 intensified (see Figures 1, 4, and 5a), but their influences persisted to later times. Instability dynamics revealing weaker dissipation of Phases 1 and T as Phase 2 intensified (Figure 6, center column) are shown at the same times at right in Figure 6 for comparison with Phase 2. Both Phases 1 and T revealed significant smaller-scale 3-D structures spanning their peak (but much weaker) brightness at 12:36 and 12:38 UT having very different character in their more western and eastern regions. Those in the western region occurred in close proximity to the remaining Phase 1 SA dynamics (see the distorted phase structure at upper left). They exhibited quite small-scale (<1 km) 3-D features in the bright portion of Phase 1 and somewhat larger 3-D structures (~ 1 km diameter) suggesting a transition to vortex rings trailing a shallower Phase T at these times that dissipated rapidly thereafter. In contrast, the

eastern portion of Phase 1 revealed very fine-scale linear features that were likely KHI that arose at a thin shear layer beneath Bore 1 as it weakened, as described above accompanying Bore 2. These features then advected southward with respect to Phases 1 and T, persisted as Phase 1 disappeared, and continued to advect beneath Phase T thereafter.

Also seen as a component of Phase T was a long, dark, larger-scale, feature that was one of several observed as early as 12:26 UT that passed through Phase T shortly after its emergence; see the bright and dark features between Phases 1 and T and the brightness variations along Phase T in the upper and center left panels in Figure 6. These features had $\lambda_h \sim 2$ km sinuous variations along their axes at the earlier times. A single phase of these structures appeared to merge with Phase T beginning $\sim 12:32$ UT and to remain aligned, become more uniform along its axis, and account for the dark Phase T “core” that persisted to later times. Unfortunately, PMC profiling of Phase T occurred ~ 20 min after these dynamics had largely abated. The initial sinuous features at earlier times resembled KHI, but they did not exhibit apparent secondary instabilities over this evolution which would have been expected. The subsequent “capture” of a single feature by the apparently decaying Phase T, and its persistence as part of Phase T over an ~ 10 -min interval as it decayed, do not resemble any GW or bore dynamics observed or modeled to date of which we are aware.

Figure 7 shows the intensification of Phase 3 and the further evolution of Phases 2 and 3 over the last 15 min of the Bore 1 event. Phase 2 exhibited a continuation of the KHI and small-scale trailing instabilities shown at earlier times in Figure 6 (center column). The KHI seen earlier intensified and initiated secondary instabilities that caused their breakdown and decay by $\sim 12:54$ UT (see the white ovals in Figure 7). Trailing instabilities that were only forming at earlier times intensified significantly by 12:48 UT, rapidly attained even smaller scales, and began to initiate small-scale 3-D structures in their wakes thereafter (see the brighter region below Phase T from 12:45–12:51 UT in Figure 7). The decreasing instability scales at later times imply a decreasing vertical scale of the forcing dynamics, based on modeling of nonlinear GW and multiscale dynamics employed in interpretations of PMC imaging (Fritts et al., 2017; F19; Miller et al., 2015).

Both Phases 2 and 3 also exhibited larger-scale variations in brightness across their axes that were similar to that seen to arise at late stages in Phase T having apparent scales of ~ 2 and 3 km. However, we are aware of no KHI modeling or observational studies that show the formation and separation of initially closely spaced KHI as they evolve. Instead, recent KHI multiscale observations suggest rapid dissipation in such cases (BF14). Hence, these features remain a mystery at this time.

The final image in Figure 7 reveals a complex nest of vortex structures, some of which can be traced to the dynamics discussed above, and others that suggest larger-scale dynamics continuing to drive additional small-scale features, despite the decay of the Bore 1 phases discussed above. In particular, additional small-scale KHI appeared to arise accompanying a resurgence of larger-scale dynamics at the location of Phase 1, despite its initial decay ~ 10 – 15 min earlier.

5. Bore 2 Analysis

5.1. Bore 2 Imaging

The large-scale Bore 2 evolution shown in PMC imaging from 13:15–13:55 UT in Figure 1 was discussed in broad terms in section 3. Zoomed views of these dynamics from 13:25–14:00 UT in the sliding rectangle labeled P2 in the projected FOV in Figure 1 are shown in Figure 8 at a 2.5-min cadence to enable a more comprehensive exploration of the detailed Bore 2 dynamics. As for Bore 1, we also quantify the evolution of the Bore 2 phase speed by averaging along phase features over 12 km E-W in a N-S swath advecting westward with the mean westward drift of the PMCs relative to the PMC Turbo payload. The swath was chosen to capture the separation of the Bore 2 peak brightness into distinct maxima at the western edge of the Camera 7 FOV at later times in Figure 8. As for Bore 1, Bore 2 brightness traces with means removed are shown in Figure 5b from 13:20–13:55 UT.

3-D structures seen in Figure 8 ahead of Bore 2 up to $\sim 13:35$ UT hint at GW instability dynamics that contributed to Bore 2 generation, as seen more clearly in the Bore 1 evolution. These features are confirmed with unprojected images in region E of the Camera 5 FOV shown at top in Figure 9. Also seen in Figure 1 was a less distinct GW phase that trailed Bore 2 by ~ 25 – 30 km at 13:35 UT, also exhibited apparent ring-like 3-D instabilities and dissipated by $\sim 13:45$ UT (see the Cameras 4 and 5 FOVs in Data S1). However, this GW

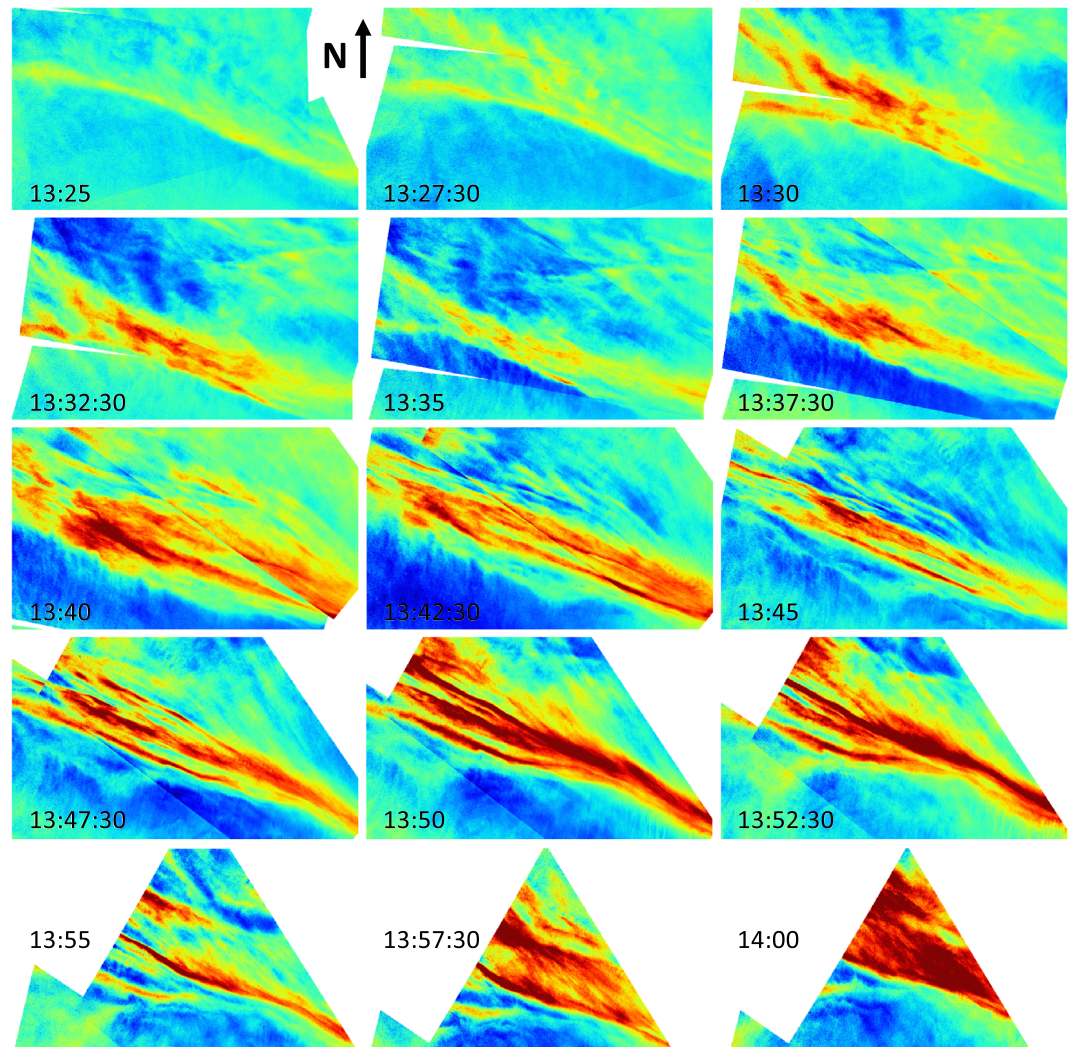


Figure 8. As in Figure 4 showing the Bore 2 evolution in region P2 in Figure 1. Note the trailing instabilities extending to late stages and the apparent multiscale KHI beginning \sim 13:30 UT.

phase was too transient and had too little PMC brightness to allow a phase speed determination. The two GW phases exhibited approximate phase alignment, and the leading phase yielded large-scale vortex rings \sim 10–30 km and \sim 10 min ahead of, and above, the Bore 2 deepest descent. Importantly, these instability dynamics (and potentially Bore 2 forcing) appeared to be stronger in the western portion of the PMC imaging FOV, and vortex rings at higher altitudes imply GW forcing at \sim 1 and 2 km or more above Bore 2.

As for Bore 1, the mean motion of the PMC layer was estimated from observed advection of small-scale features. Features ahead of Bore 2 at the upper edge of the Cameras 5 and 6 FOVs advected toward \sim 5–15°N of W at 58 ± 6 m/s between 13:20 and 13:30 UT. Features trailing Bore 2 revealed advection largely toward W at 50 ± 5 m/s between 13:40 and 13:50 UT. Bore 2 inferred phase speeds toward 25° east of north at earlier and later times were thus \sim 44 and 55 m/s, respectively. However, the altitude of, and mean wind at, the Bore 2 duct cannot be inferred from these observations.

Bore 2 intensified and narrowed quickly, attaining a bright full width of \sim 8–10 km by \sim 13:35 UT accompanying its deepest descent. Bore 2 imaging also revealed modulation of the bright phase by brighter and darker undular features aligned along Bore 2 that had E-W $\lambda_h \sim 2$ and 3 km, as seen to accompany Bore 1 and discussed above (see Data S1). As for Bore 1, these features were apparent KHI advecting beneath Bore 2 at

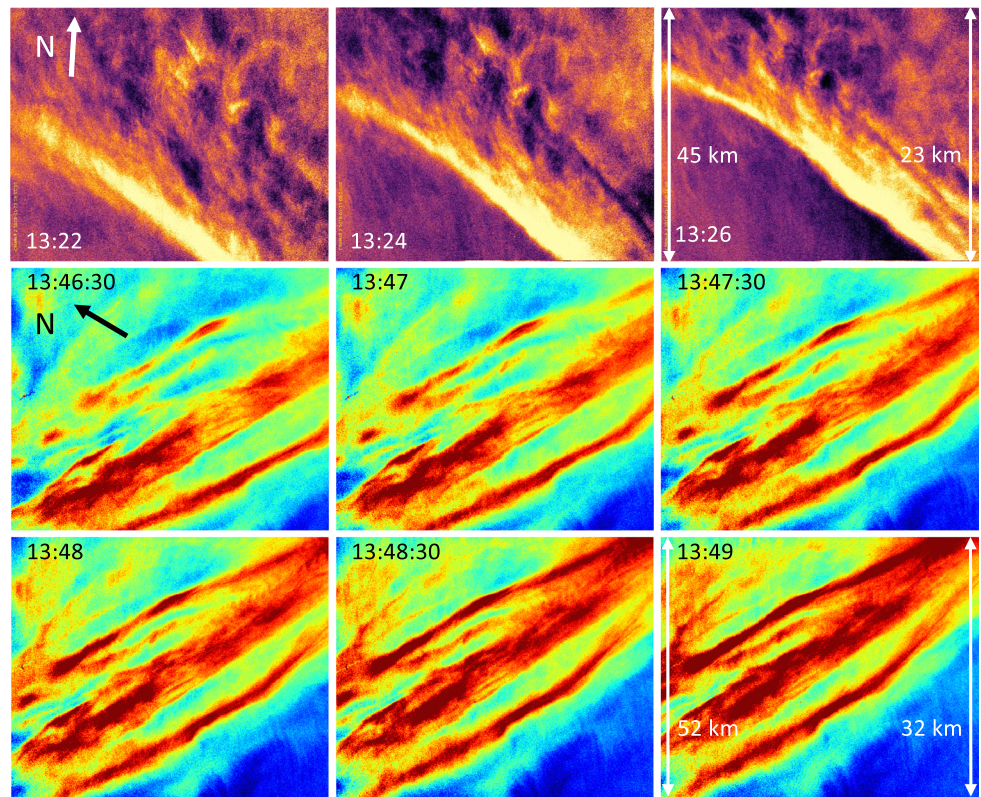


Figure 9. (top) Camera 5 imaging of vortex rings ahead of the Bore 2 as it intensifies. (bottom) Camera 7 imaging of large-scale KHI and secondary KHI at late stages of the Bore 2 evolution at large zenith angles. Color scales at top (bottom) are as in Figures 5 and 1, respectively.

these times. The KHI in this case had $\lambda_h \sim 2$ and 3 km and likewise were seen to advect rearward beneath the initial solitary Bore 2 phase at earlier times (see the merged FOV imaging from $\sim 13:30$ – $13:45$ UT in Figure 8). Thereafter, Bore 2 evolved differently along its phase in the merged FOV. It remained relatively confined N-S to the E where initial forcing appeared to be weaker, but exhibited widening of the bright phase by $\sim 13:40$ UT. It then evolved multiple, separate brightness maxima that dispersed further at later times (see Figure 8 and the lower two rows of Figure 9), suggesting transition to an undular bore. Importantly, perhaps, the central, broader bright feature exhibited clear modulations having $\lambda_h \sim 2$ and 3 km, as seen at earlier times, and smaller-scale $\lambda_h \sim 500$ m to 1 km features aligned with the larger-scale bore brightness maxima that were likely larger-scale secondary KHI at these times and locations. Similar smaller-scale features aligned with the larger-scale bore components also persisted to later times even as the overall field appeared to break down and become more uniform along the direction of Bore 2 propagation.

5.2. Bore 2 BOLIDE Profiling

Section 3 provided an overview of BOLIDE profiling contributions to defining large- and smaller-scale Bore 2 structure and behavior. Here, we employ PMC and T' profiling to aid our interpretation of Bore 2 generation, evolution, and dissipation at smaller spatial and temporal scales. In this case, the bright PMC layer was apparently modulated in altitude by GWs having observed periods of ~ 1 hr and ~ 15 – 17 min, both of which may have contributed to Bore 2 peak descent of ~ 1 km at $\sim 13:34$ UT (see Figures 2b and 2e). The bright portion of the PMC layer was relatively thin at this time, with a width of ~ 100 – 200 m, so was a reliable tracer of small-scale motions at these times.

BOLIDE PMC profiling sensitivity over this interval revealed ~ 2 and 3 min oscillations at ~ 80 km spanning ~ 10 – 15 min prior to Bore 2 passage. These oscillations are consistent with the advection speed and spatial scales of the vortex rings seen in PMC imaging shown at top in Figure 9 (which represent the first

compelling lidar observations of vortex rings). Additionally, these altitude variations decreased strongly as Bore 2 approached, and the observed vortex rings subsided at the location of lidar profiling at ~13:24 UT. Note that the lidar profiling was ~5 km E of the NE edge of the PMC images at top in Figure 9 (see Figure 1, region E, at 13:25 UT).

As seen in the PMC profiling of Bore 1, that for Bore 2 also provided evidence of descending tendrils of brighter PMCs beneath the Bore 2 deepest descent. In the Bore 2 case, these were not as bright and clearly defined because Bore 2 exhibited more variable brightness at the time of deepest descent, and the peak brightness was confined to somewhat higher altitudes. Nevertheless, several tendrils were seen to extend as far as ~500 m to over 1 km below the apparent Bore 2 deepest descent. The implications of these observations for instabilities are described below.

Finally, Rayleigh lidar measurements of T' revealed observed GW periods of ~30 min to 2 hr that likely had amplitudes sufficient to induce instabilities above ~70–75 km, and which could have contributed to Bore 2 forcing or the environment in which it arose. But there is no clear evidence of an ~1-hr GW that may have accounted for the bore spacing in time. Additionally, lidar T' measurements revealed GWs having apparent ascending phases and periods of ~30–60 min extending from ~12–18 UT that have two possible interpretations. Either they are evidence of GWs propagating upward toward E, but with intrinsic phase speeds that are less than the mean westward motion at these altitudes, hence had observed ascending rather than descending phases. Or they are evidence of true, downward-propagating GWs that were propagating more nearly in the plane of bore propagation, hence had apparent upward phase progression. Given that there was no clear evidence in PMC imaging for GW propagation in a roughly E-W plane, we conclude that the most plausible explanation for ascending GW phases is GW radiation to lower and presumably higher, altitudes contributing to bore dissipation.

5.3. Bore 2 Instability Dynamics

We noted in section 5.1 the evidence for GW forcing of Bore 2 via a GW having $\lambda_h \sim 25\text{--}30$ km, an apparent strong breaking phase accompanying Bore 2 generation, and a weaker but also unstable trailing phase. Vortex rings accompanying the strong phase shown over 4 min in the top row in Figure 9 had diameters as large as ~6–8 km, so were comparable to or larger than seen for the Bore 1 forcing by localized 3-D GW SA dynamics. The vortex ring relative alignments seen at top in Figure 9 suggest that the GW was aligned roughly N-S, so $<30^\circ$ counter-clockwise from the emerging Bore 2 bright phase orientation. They also exhibited closely spaced overlapping structures, suggesting a relatively high-frequency GW source and implied rapid and large momentum deposition. The larger vortex ring diameters further suggest a GW $\lambda_z \sim 20$ km that is in agreement with modeling of GW breaking at high intrinsic frequencies (Fritts, Wang, et al., 2019). Importantly, however, and as noted for Bore 1, the vortex rings occurred above the Bore 2 bright phase, hence suggest that the major forcing and momentum deposition was at higher altitudes than the primary Bore 2 response.

Two types of instabilities occurred nearly continuously throughout the Bore 2 evolution: larger- and smaller-scale KHI and trailing instabilities. At intermediate times from ~13:32:30–13:42:30 UT (see Figure 8), Bore 2 generally thinned and intensified, but continued to exhibit larger-scale ($\lambda_h \sim 2$ and 3 km) KHI that were entrained and intensified as they passed beneath Bore 2, led to bright descending PMC tendrils during the deepest Bore 2 descent, and continued as Bore 2 intensified. These larger-scale KHI persisted as Bore 2 fragmented; see the smaller-scale ~linear structures aligned along the Bore 2 component axes from 13:42:30–13:52:30 UT and thereafter. Bore 2 also exhibited apparent secondary KHI at smaller scales that can only arise for strong KHI having low to intermediate Ri and high Re . These are seen in the projected images at center and right in the bottom row of Figure 9 and with better resolution in the white ovals in Figure 10.

Also seen in the Bore 2 structure in Figure 8 as early as 13:35 UT, at earlier and later times shown in Figure 9, and more clearly below the Bore 2 bright phase in Figure 10 beginning at ~13:48 UT, are small-scale trailing instabilities having alignments roughly normal to the primary Bore 2 bright phase. These features arose initially at the western edge of the PMC imaging and intensified quickly. Thereafter, Bore 2 apparently diminished in its intensity and dispersed along its propagation direction (as an apparent, successive undular bore) following the earlier occurrence of trailing instability dynamics further to the west. However, small-

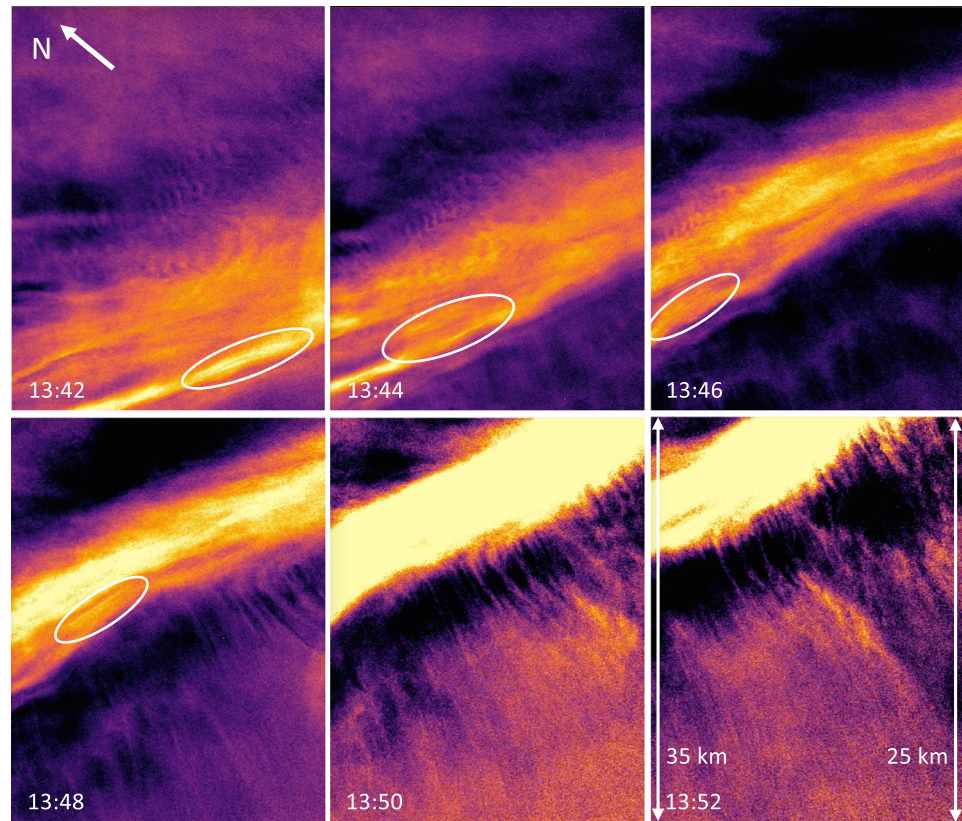


Figure 10. Camera 7 imaging of Bore 2 dissipation at its leading and trailing edges (top and bottom of each panel) at late stages of its evolution at small zenith angles. Color scale is as in Figure 5.

scale trailing instabilities clearly extended from $\sim 13:35$ UT to the latest stages of the Bore 2 evolution, hence likely contributed to Bore 2 dissipation throughout its evolution.

6. Discussion

Our analyses of the two bore events described here include many inferences of GW and instability dynamics contributing to their forcing, features, character, and evolutions. In many cases, these inferences are robust and justified based on similar features seen in previous bore observations and modeling and observations of idealized, multiscale, and SA GW dynamics and KHI. Others are based on much more limited bore theory and modeling, which suggest tantalizing diversity, but few robust conclusions to date. The major factors enabling quantitative and confident identification of specific features in a number of cases were the simultaneous, common-volume, high-resolution PMC Turbo imaging and profiling, and previous modeling describing the primary instability dynamics. Examples include (1) simultaneous horizontal and vertical definition of bore vertical displacements and horizontal scales, (2) distinctions between the altitudes of GW instabilities driving bore forcing and the adjacent bore responses, and (3) identification of the various GW and KH instabilities that play important roles in bore formation, evolution, and dissipation.

Observed GW and instability dynamics discussed here in which we have high confidence based on various modeling efforts include the following:

- 1) localized small-scale SA dynamics contributing to forcing of Bore 1,
- 2) strong GW breaking at $\lambda_h \sim 25\text{--}30$ km apparently forcing Bore 2,
- 3) vortex rings that provide insights into GW λ_z and ω_i ,
- 4) widely occurring trailing instabilities, and
- 5) the larger-scale KHI and smaller-scale secondary KHI for which there is observational support in another PMC Turbo analysis in preparation.

Instabilities and dissipation are not restricted to the formation stages of the two bores, but are an expected property of all bores throughout the various stages of their evolutions (Rayleigh, 1908). Early bore theory identified two forms: turbulent (or foaming) bores and undular bores (DP98, Tricker, 1965; L79). Importantly, our results for Bore 1 suggest that an initial, potential solitary bore can yield an undular bore as a consequence of its initial decay in the event that forcing is not sufficiently strong to yield an internal solitary wave response. Likewise, Bore 2 exhibited a more likely solitary wave response having associated instabilities throughout its evolution, thus more like a turbulent solitary bore that appeared to decay to a successive undular bore as it lost energy.

Clear variations in the two bore evolutions at earlier and later times suggest different bore formation dynamics, environmental influences, character, and evolutions. The most conspicuous difference identified in section 3 is the apparent undular bore character of Bore 1, and the more likely solitary wave character of Bore 2 just noted. Additional differences revealed in PMC imaging (compare Figures 4 and 8, and Figures 5a and 5b) include the following:

1. Bore 1 appeared to arise in response to strong, local GW SA dynamics whereas Bore 2 arose accompanying more extended GW breaking that did not exhibit obvious, localized SA dynamics,
2. Bore 1 exhibited almost immediate emergence of leading and trailing phases, while Bore 2 contracted horizontally and coalesced for ~30 min at smaller zenith angles, and only exhibited apparent emerging additional bright phases after ~20 min,
3. Bore 1 Phase 1 phase speed decreased after ~20 min, while that for Bore 2 increased,
4. Bore 1 Phase 1 brightness decreased with time, while that for Bore 2 increased initially,
5. successive Bore 1 leading phases exhibited λ_h contraction after formation, while successive Bore 2 phases exhibited apparent λ_h expansion, and
6. Bore 1 (Bore 2) exhibited relatively weaker (stronger) KHI intensities, entrainment, and secondary KHI throughout their evolutions.

These apparently significant differences in bore character suggest that potentially small differences in propagation environments (or ducting character) and/or the strength of formation dynamics can lead to significantly different evolutions and MLT impacts. Additional comparisons between Bores 1 and 2 observed in BOLIDE PMC profiling and instability dynamics are explored below.

A representation of Bore 1 spatial variations and observed and inferred motions implied by PMC imaging and BOLIDE profiling is shown in Figure 11 for bore propagation to the left (as in Figure 2b). If this is a reasonable approximation of Bore 1 structure at this time, the variable vertical extent of the PMC layer implied horizontal (vertical) convergence (divergence) ahead of Bore 1 phase passage and horizontal (vertical) divergence (convergence) behind Bore 1 phase passage. Arrows in Figure 11 are intended to approximate these flows, with thicker arrows implying stronger flows and solid (dashed) lines indicating observed (inferred) Bore 1 features, phase speed, and meridional wind. The variable inferred directions along the Bore 1 axis are suggestive of the variable flows implied by multiple crests of an undular bore in the initial theoretical studies (DP98, DP01) and limited modeling performed to date (L09; L11; G15).

The inferred vertical divergence (convergence) ahead of (behind) Bore 1 Phase 2 implies decreasing (increasing) T and airglow brightness ahead and above (below) and behind and below (above), as noted for the initial “wall” wave observed by Taylor et al. (1995) and Swenson et al. (1998) and in multiple bore observations thereafter. Swenson et al. (1998) also noted an increase in Na column density and significant warming accompanying bore passage. Similar responses in Na column density accompanying large downward displacements and warming were also seen by Batista et al. (2002), Smith et al. (2005), and Li et al. (2013), though in these cases they spanned a few hour.

Smith et al. (2005) argued that the bore in that case arose due to GW breaking at $\lambda_h \sim 28$ km and implying momentum deposition leading to bore formation thereafter, as initially proposed by DP01. The opposite O(¹S) and OH airglow bright and dark peaks at later time are coincident in time and likewise bear a close resemblance to the measured vertical displacements seen in Figure 2c and depicted in Figure 11, thus agree closely with those of Bore 1. As discussed in section 4, Bore 1 exhibited emergence of three leading crests ahead of Phase 1, all of which experienced a systematic decrease in their spacing from the preceding crest subsequent to their formation. Bore 1 also exhibited emergence of a trailing crest as

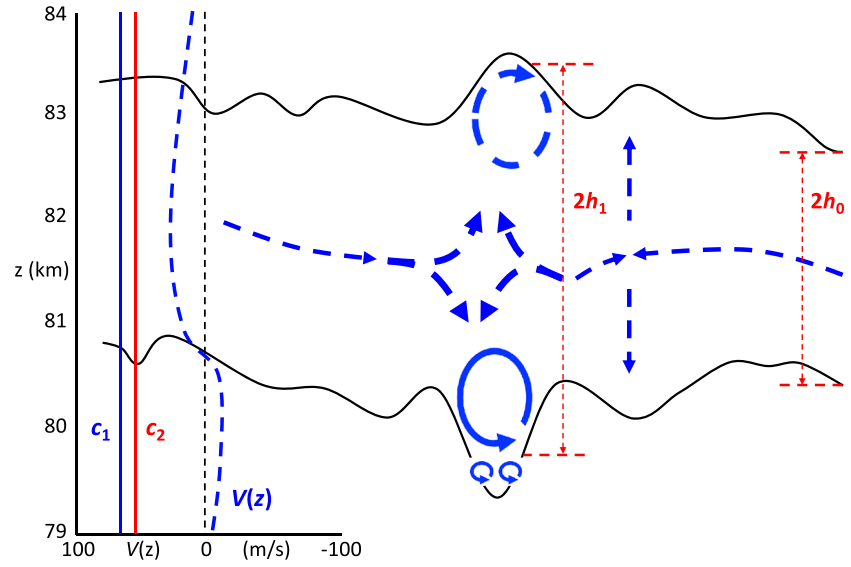


Figure 11. Observed (solid lines) and hypothesized (dashed lines) motions accompanying observed vertical displacements of Bore 1 based on PMC profiling spanning its passage and assuming no temporal evolution over this interval, which is surely too simplistic. The profile at left shows a hypothetical meridional wind, $V(z)$, that is roughly consistent with NAVGEM reanalysis above ~ 81 km and could account for bore Doppler ducting and the relative phase speeds of the Bore 1 Phases 1 and 2, c_1 and c_2 . Dashed red lines at right denote the estimated “channel” depths, respectively, at the bore response and in the background atmosphere (see text for details).

Phase 1 began to diminish in amplitude. These features suggest the excitation of an undular bore from a large initial nonlinear response to strong local GW SA dynamics and forcing exhibiting only a single initial bright phase.

Referring to Figure 11 and employing the terminology of L79 and DP98, we estimate a ratio of the bore layer depth at the peak response ($2h_1 \sim 4.7$ km) to that in the trailing field at the right edge ($2h_0 \sim 2.8$ km) as $h_1/h_0 \sim 1.7$ and a normalized bore amplitude, $\beta = (h_1 - h_0)/h_0 \sim 0.7$ (DP98, Equation 6). This estimate is larger than the expected threshold for transition from a strong, nonlinear (and turbulent) solitary wave to an undular bore in this theory, hence appears to suggest that a solitary wave may have arisen, had the duct been a thermal duct. The amplitude seen in lidar profiling is also significantly smaller than that inferred to accompany the much stronger response in PMC imaging further west. Thus, the L79 and DP98 theory for a thermal duct seems not consistent with the observed evolution. This is speculative, however, because neither theory nor modeling has yet established the different responses that arise for differing forcing character and intensity, duct character, and external environmental stratification. Additionally, no modeling has yet been performed addressing bore forcing by localized 3-D GW breaking or SA dynamics.

DP98 (Equations 12 and 13) theory estimates an undular bore horizontal wavenumber and intrinsic phase speed, k_h and c_i , as

$$k_h = 2\pi/\lambda_h = (3/h_1)[(h_1 - h_0)/2h_0]^{1/2} \quad (1)$$

and

$$c_i^2 = g'h_1(h_1 + h_0)/2h_0 \quad (2)$$

where $g' = g\Delta\theta/\theta$, $g \sim 9.5$ m/s² is the gravitational constant, and θ and $\Delta\theta$ are the mean potential temperature at the bore duct and half the difference across the ducting layer. Equation 1 implies a Bore 1 $\lambda_h \sim 10.4$ km, which is comparable to that seen in GW SA dynamics at early times. However, the GW SA dynamics inferred from our PMC imaging is highly nonlinear and dissipative, not steady, nor does it lead to a succession of undular bore phases that exhibit constant λ_h and c_i . Thus, the DP98 thermal

duct theory appears not to provide a viable explanation for Bore 1 structure and evolution, and Bore 1 structure suggests instead a more complex ducting environment.

Bore 2 forcing was likewise apparently dependent on strong GW breaking and local momentum deposition. Unlike Bore 1, however, Bore 2 forcing extended across the entire E-W imaging FOV, but achieved the largest apparent influences at more central locations. As for Bore 1, Bore 2 forcing accompanied large-scale, closely spaced and overlapping vortex rings having diameters as large as $\sim 6\text{--}8$ km immediately preceding the emerging bright initial bore phase. The bright phase overtook multiple, bright vortex rings apparently at nearly the same altitude as it approached the location of lidar profiling, which indicated that the dynamics ahead of Bore 2 most likely occurred at ~ 80 km and above. In this case, however, the initial GW λ_h was not well defined, but likely had $\lambda_h \sim 25\text{--}30$ km, given a trailing unstable phase that was less well defined due to much weaker PMCs apparently at a significantly higher altitude.

The Bore 2 single-phase response persisted for ~ 20 min and suggests a strongly turbulent solitary wave until it transitioned to multiple, separate phases that separated and dispersed thereafter, especially at its western edge. The apparent transition from a solitary wave to an undular bore was in rough agreement with L79 and DP98 predictions, but the separation of the resulting phases was not. Thus, the Bore 2 evolution also suggests a more complex ducting environment than a simple thermal duct, especially given the strong shear at its lower edge demonstrated by strong KHI and the implied momentum deposition at or near the apparent Bore 2 ducting altitude.

We explore potential explanations for Bore 1 and 2 evolutions and quantitative aspects of their responses more fully by employing reanalysis results obtained with the U.S. NAVy Global Environment Model (NAVgEM). NAVgEM now employs a new hybrid 4-D variational (4DVAR) T119 L74 data assimilation procedure (Eckermann et al., 2019) that was recently extended to include global MLT radar winds at $\sim 80\text{--}100$ km from 25 sites. The resolution yields a Nyquist scale of ~ 134 km at the location of PMC Turbo observations, hence is expected to account for GWs arising from meteorological sources at lower altitudes having $\lambda_h \sim 300$ km and larger. The new NAVgEM reanalysis was tested by comparison with meteor radar winds over ALOMAR in N. Norway employed as part of the reanalysis effort and to characterize the large-scale winds during PMC Turbo as described by Fritts, Miller, et al. (2019) and at other sites.

To validate the NAVgEM reanalysis for our purposes here, we compare observed PMC advection with local NAVgEM winds at 66.5°N , 97°W . The NAVgEM U , V , T , and N profiles at 12, 13, and 14 UT are shown in Figure 12. As noted above, three PMC advection estimates from 11:55–12:30 UT suggested a mean motion of 62 ± 6 m/s toward $5\text{--}10^\circ$ S of W, which appear to be in close agreement with the NAVgEM winds at the brightest PMC response at ~ 80 and 81 km at these times shown in Figures 12a and 12b. The apparent decreasing southward component of the PMC layer drift speed at these times ($\sim 12:30$ UT) is also consistent with increasing V to small positive values in NAVgEM from 12–13 UT at these altitudes. These comparisons give confidence in the use of NAVgEM winds for our bore analysis. NAVgEM also yielded very reasonable T and N profiles at this latitude and season. A weak local N maximum at 89 km evolves by 13 UT, but has larger $N \sim 5$ km above, thus seems not a viable thermal duct without wind influences.

Returning to our bore analyses, we note that smaller-scale and higher-frequency GWs having observed periods of ~ 1 hr and less, as indicated by the horizontal convergence and divergence of the PMC layer, and its vertical displacements, seen in lidar profiling of PMCs in Figure 2a and of T' in Figure 6, were surely also present. However, GWs having λ_h resolved by PMC Turbo imaging appeared only to be significant during bore forcing, and well or somewhat west of lidar profiling in each case. Lidar profiling from 12:00–13:30 UT in Figure 2a reveals only small vertical displacements of the PMC layer, apart from the bores themselves. These imply amplitudes of $u' \sim (g/N)(T'/T) \sim 9$ m/s (for hydrostatic GWs) with $T' \sim 2.5$ K for a peak vertical displacement of $\delta z \sim 500$ m. The good agreement of NAVgEM winds with inferred PMC advection and the absence of other resolved GWs at these times, provide further confidence in the use of NAVgEM fields as an approximate guide for our interpretation of the dynamics accompanying the bore evolutions.

The Bore 1 estimate of the initial GW phase speed in the western portion of the PMC imaging from Figures 3 and 4a, $\sim 65 \pm 6$ m/s relative to the PMC layer, was $\sim 50\text{--}60$ m/s faster than the NAVgEM V from $\sim 60\text{--}90$ km between 12 and 13 UT. For our purposes here, we assume a more conservative value of ~ 40 m/s faster, given that local accelerations in the direction of GW propagation precede SA and instability dynamics. These

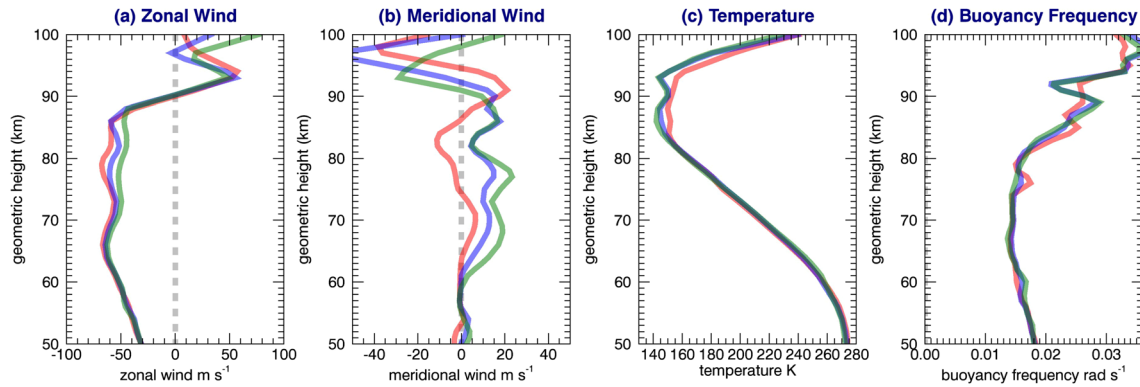


Figure 12. NAVGEM reanalysis profiles of (a-d) U , V , T , and N^2 at 66.5°N , 97°W at (red, blue, and green) 12, 13, and 14 UT on 13 July 2018. The NAVGEM reanalysis was performed at T119, L74 resolution, so resolves GW scales ~ 300 km and larger.

values yield smaller (and more conservative) estimates for various GW parameters, with larger values likely but not certain. With this assumption, the implications of the various observations and NAVGEM reanalysis for GW structure and Bore 1 forcing include the following:

- 1 a GW having a large amplitude ($a = |u_h'/c_i| > 1$) and $c_i \sim 40$ m/s exhibited SA dynamics and strong breaking over a significant depth at and below the PMC layer accompanying the apparent forcing of Bore 1,
- 2 the GW observed $\lambda_h \sim 13$ km and inferred $\lambda_z \sim 15\text{--}20$ km are consistent with vortex ring diameters of $\sim 5\text{--}7$ km, close ring spacings and overlaps, and $\omega_i^2 > N^2/2$ observed during Bore 1 forcing (Figure 5, left). They are also very similar to those seen in previous ground-based PMC and airglow imaging (Fritts, Wang, et al., 2019) and anticipated by high-resolution modeling of GW breaking at $|u_h'/c_i| \sim 1$ and large ω_i (Fechine et al., 2009b, Fritts et al., 2019),
- 3 the very high GW ω_i would have prevented propagation significantly above ~ 90 km due to increasing ω_i approaching N accompanying increasing southward V and $c_i = (c-V)$.
- 4 $N^2(z)$ profiles in Figure 12 exhibit no strong and sustained maxima below 100 km that would have accounted for a thermal duct,
- 5 phase-averaged peak GW momentum fluxes were $\langle u_h'w' \rangle \sim 920$ m²/s² or larger, hence among the largest estimates obtained in the MLT to date,
- 6 GW breaking and SA dynamics yielded very strong local body forcing with an expected peak $dV/dt \sim \langle u_h'w' \rangle / H \sim 14$ m/s/min (for local scale height $H \sim 4$ km) at GW breaking altitudes below the strong negative V above ~ 90 km, and
- 7 an induced jet in V above the Bore 1 phase descents arising from GW breaking and SA dynamics that contributed to a velocity duct enabling Bore 1 ducting thereafter.

Bore 2 experienced a more eastward U and a more northward V , propagated toward $\sim 25^\circ$ east of north, and had an initial phase speed relative to the PMC layer of ~ 44 m/s that increased to ~ 55 m/s after $\sim 13:35$ UT. These observations implied $c_i \sim 35$ m/s relative to winds at $\sim 65\text{--}80$ km as Bore 2 intensified and decreased in width, and c_i increased to ~ 45 m/s as Bore 2 expanded and dissipated thereafter. Additional elements of the Bore 2 evolution providing clues to its forcing and ducting character include the following:

- 1 a breaking GW having vortex ring diameters as large as $\sim 6\text{--}8$ km above the bore altitude, $a = |u_h'/c_i| > 1$, an implied $\lambda_z \sim 15\text{--}20$ km, and an observed $\lambda_h \sim 25\text{--}30$ km,
- 2 an inferred non-hydrostatic GW having $\omega_i^2 \sim 0.2\text{--}0.3N^2$ that had closely spaced vortex rings, a more extended E-W response than seen for Bore 1, and which did not exhibit SA dynamics at the PMC layer,
- 3 phase-averaged peak GW momentum fluxes that were at least $\langle u_h'w' \rangle \sim 300$ m²/s², and
- 4 local momentum deposition and flow accelerations along the initial GW propagation direction of $dU_h/dt \sim \langle u_h'w' \rangle / H \sim 5$ m/s/min that likely contributed to the character of the Bore 2 duct at $\sim 82\text{--}90$ km.

Bore features identified above reveal quantitative differences in forcing and evolutions in the two events, and also multiple common features. The differences can be at least partly attributed to the identified differences in GW forcing dynamics, likely including different forcing intensities, spatial and temporal event scales, and

to somewhat different thermal and wind environments. Common features include similar responses in PMC lidar profiling suggestive of a large-scale GW having an ~ 1 -hr period contributing to the bore environment and potential initiation, forcing by small-scale GW breaking or local SA events, the presence and apparent significance of KHI (and implied energy dissipation) accompanying both events, formation of successive bright phases during their decay, and evidence in each case for behavior not consistent with a thermal duct. For reference, another similar event was observed at $\sim 14:30$ UT that also exhibited strong GW breaking at its inception, but failed to yield clear, persistent brightness maxima thereafter, and which was less well defined in PMC imaging and profiling (see Figure 2a).

Inferred strong local forcing accounting for Bores 1 and 2 excitation implied local flow accelerations that must have resulted in an augmented jet along the bore propagation direction at higher altitudes than the major bore responses. Our observations support the suggestion of bore forcing by a breaking GW by Smith et al. (2005). The inference of bore phase evolutions that depart from the theory for thermal ducts (DP98) also provide evidence for a Doppler or mixed thermal-Doppler duct as suggested in limited modeling to date (L09).

Finally, the apparent continuous occurrence of KHI that accompanied Bores 1 and 2 is likely not typical of general bores, especially where they are supported by thermal ducts without significant associated wind shears. In these cases, however, they appear to have occurred on a strong local wind shear that was present in the background wind field and enabled sufficiently low Ri to initiate local KHI in various regions, and which intensified where the descending bore phases compressed the shear and reduced $Ri = N^2/(dV/dz)^2$. This occurs because N^2 and dV/dz both increase linearly with compression in the vertical, but this would not occur for large Ri in a weakly sheared flow.

7. Summary and Conclusions

Observations performed by PMC Turbo on 13 July 2018 enabled quantification of bore dynamics in the MLT that are challenging or impossible to identify or describe with confidence using previous ground-based or other instrumentation. These results were consequences of colocated high-resolution imaging and profiling that took advantage of a unique “window on small-scale dynamics” that does not occur anywhere else in the atmosphere, nor in any other fluid of which we are aware. This capability arises because the brightest part of the PMC layer is often as thin as ~ 100 m and frequently as thin as a few 10's of m when small-scale dynamics are strong (Fritts et al., 2017), thus enabling imaging of GW, instability, and turbulence structures as small as ~ 20 – 50 m. Importantly, the expected inner scale of turbulence, l_0 , is as small as ~ 10 – 20 m at the PMC altitude. Hence, PMC high-resolution imaging and profiling offers the potential to follow and quantify the flow of energy from larger-scale GW dynamics that account for energy and momentum transport into the MLT, through the instabilities accounting for GW breaking, and extending to the turbulence scales accounting for energy dissipation. The implications are that combined high-resolution PMC imaging and profiling can provide key insights into important small-scale dynamics that cannot be obtained with any other methods at present.

Specific results of our bore analyses employing these capabilities include the following:

- 1 Observations of apparent horizontal convergence, deep lower-edge descents, and apparent strong shearing and KHI at the lower edge accompanying bore passage,
- 2 Documentation of apparent bore forcing by large-amplitude GWs having $\lambda_h \sim 12$ – 30 km undergoing breaking and/or SA and implying strong momentum deposition,
- 3 Quantification of the phase evolution of an apparent undular bore (Bore 1) exhibiting leading and trailing phase formation, leading phase shrinking, and decay spanning ~ 1 hr,
- 4 Quantification of the formation, intensification, and eventual splitting, continuous KHI, and dissipation of an apparent initial internal solitary wave (Bore 2) spanning ~ 40 min,
- 5 Evidence supporting the bore responses inferred in previous studies, especially horizontal convergence (divergence) leading to brighter and warmer (darker and cooler) bore features and corresponding leading (trailing) edge vertical divergence (convergence) and implied T (airglow brightness) responses above (below) the bore duct, and
- 6 Observations revealing that both bores exhibited trailing instabilities and energy dissipation throughout their evolutions.

Broader implications of our bore study include the following:

- 1 Qualitative confirmation of a number of predictions of mesospheric bore theory (DP98, DP01) regarding leading phase generation, bore amplitudes and transitions, responses at higher and lower altitudes, and dissipation throughout the events,
- 2 Evidence of phase compression (decreasing λ_h) in Bore 1 that is not predicted by bore theory and instead suggests a Doppler or mixed thermal-Doppler duct (L09), and
- 3 Evidence of an asymmetric form within the Bore 1 response about the likely duct altitude also suggesting a more complex ducting environment (L09).

Finally, we note that apparent bores were not infrequent during the short PMC Turbo flight, suggesting that they may be more dynamically relevant than previously believed. This is especially the case given their potentially significant roles in generation of instabilities leading to turbulence and mixing where they occur. Because dynamics enabling bore formation are likely prevalent throughout the atmosphere (specifically, highly structured flows and strong GW forcing can occur from the troposphere into the MLT), and bores imply strong local instabilities and mixing, they may play more significant roles in energy and momentum transport and deposition throughout the atmosphere than has been appreciated to date.

Summarizing, bores in the MLT arise due to strong forcing of a conducive duct composed of one (or several) local maxima in N^2 and/or U_h yielding a thermal, Doppler, or mixed thermal-Doppler duct. Theory and idealized modeling to date have revealed that undular bores can arise from large-amplitude GWs impinging on a duct that steepens and evolves a series of peaks at much smaller λ_h (L09, L11, G15). Importantly, however, modeling has not yet addressed the generation of bores by local body forces, for which there is now significant observational evidence provided by Smith et al. (2005) and in the results described above.

Acknowledgments

Research described here was supported under the NASA grant cited in GEMS. This project also received funding from the German Aerospace Center (DLR) for construction, integration, and operation of the Rayleigh lidar and subsequent data analyses. Links to data required to replicate all PMC Turbo images and other figures in this paper are available in the supporting information. Movies and figures cited in the text are available as Supplemental Materials, and data files from which figures were constructed are provided at <https://halo-db.pa.op.dlr.de/mission/112>.

References

- Bageston, J. V., Wrasse, C. M., Batista, P. P., Hibbins, R. E., Fritts, D. C., Gobbi, D., & Andrioli, V. F. (2011). Observation of a mesospheric front in a thermal-doppler duct over King George Island, Antarctica. *Atmospheric Chemistry and Physics*, *11*, 12,137–12,147. <https://doi.org/10.5194/acp-11-12137-2011>
- Bageston, J. V., Wrasse, C. M., Hibbins, R. E., Batista, P. P., Gobbi, D., Takahashi, H., et al. (2011). Case study of a mesospheric wall event over Ferraz station, Antarctica (62 S). *Annales de Geophysique*, *29*, 209–219. <https://doi.org/10.5194/angeo-29-209-2011>
- Batista, P. P., Clemesha, B. R., Simonich, D. M., Taylor, M. J., Takahashi, H., Gobbi, D., et al. (2002). Simultaneous lidar observation of a sporadic sodium layer, a “wall” event in the OH and OI5577 airglow images and the meteor winds. *Journal of Atmospheric and Solar - Terrestrial Physics*, *64*, 1327–1335. [https://doi.org/10.1016/S1364-6826\(02\)00116-5](https://doi.org/10.1016/S1364-6826(02)00116-5)
- Benjamin, T. B. (1967). Internal waves of permanent form in fluids of great depth. *Journal of Fluid Mechanics*, *29*, 559–592. <https://doi.org/10.1017/S002211206700103X>
- Brown, L. B., Gerrard, A. J., Meriwether, J. W., & Makela, J. J. (2004). All-sky imaging observations of mesospheric fronts in OI 557.7 nm and broadband OH airglow emissions: Analysis of frontal structure, atmospheric background conditions, and potential sourcing mechanisms. *Journal of Geophysical Research*, *109*, D19104. <https://doi.org/10.1029/2003JD004223>
- Chimonas, G., Hauser, H. M., & Bennett, R. D. (1996). The excitation of ducted modes by passing internal waves. *Physics of Fluids*, *8*(6), 1486–1505.
- Chimonas, G., & Hines, C. O. (1986). Doppler ducting of atmospheric gravity waves. *Journal of Geophysical Research*, *91*, 1219–1230.
- Christie, D. R. (1989). Long nonlinear waves in the lower atmosphere. *Journal of the Atmospheric Sciences*, *46*, 1462–1491. [https://doi.org/10.1175/1520-0469\(1989\)046%3C1462:LNWITL%3E2.0.CO;2](https://doi.org/10.1175/1520-0469(1989)046%3C1462:LNWITL%3E2.0.CO;2)
- Dalin, P., Connors, M., Schofield, I., Dubietis, A., Pertsev, N., Perminov, V., et al. (2013). First common volume ground-based and space measurements of the mesospheric front in noctilucent clouds. *Geophysical Research Letters*, *40*, 6399–6404. <https://doi.org/10.1002/2013GL058553>
- Davis, R. E., & Acrivos, A. (1967). Solitary internal waves in deep water. *Journal of Fluid Mechanics*, *29*, 593–607. <https://doi.org/10.1017/S0022112067001041>
- Dewan, E. M., & Picard, R. H. (1998). Mesospheric bores. *Journal of Geophysical Research*, *103*, 6295–6305. <https://doi.org/10.1029/97JD02498>
- Dewan, E. M., & Picard, R. H. (2001). On the origin of mesospheric bores. *Journal of Geophysical Research*, *106*, 6295–6305. <https://doi.org/10.1029/2000JD900697>
- Eckermann, S. D., Doyle, J. D., Reinecke, P. A., Reynolds, C. A., Smith, R. B., Fritts, D. C., & Dörnbrack, A. (2019). Stratospheric Gravity Wave Products from Satellite Infrared Nadir Radiances in the Planning, Execution, and Validation of Aircraft Measurements during DEEPWAVE. *Journal of Applied Meteorology and Climatology*, *58*, 2049–2075. <https://doi.org/10.1175/JAMC-D-19-0015.1>
- Fechine, J., Medeiros, A. F., Buriti, R. A., Takahashi, H., & Gobbi, D. (2005). Mesospheric bore events in the equatorial middle atmosphere. *Journal of Atmospheric and Solar - Terrestrial Physics*, *67*, 1774–1778. <https://doi.org/10.1016/j.jastp.2005.04.006>
- Fechine, J., Wrasse, C. M., Takahashi, H., Medeiros, A. F., Batista, P. P., Clemesha, B. R., et al. (2009b). First observation of an undular mesospheric bore in a Doppler duct. *Annales de Geophysique*, *27*(4), 1399–1406. <https://doi.org/10.5194/angeo-27-1399-2009>
- Fechine, J., Wrasse, C. M., Takahashi, H., Medeiros, A. F., Batista, P. P., Clemesha, B. R., et al. (2009a). Mesospheric bore event during SpreadFEx campaign. *Annales de Geophysique*.
- Fritts, D. C., Baumgarten, G., Wan, K., Werne, J., & Lund, T. (2014). Quantifying Kelvin-Helmholtz instability dynamics observed in noctilucent clouds: 2. Modeling and interpretation of observations. *Journal of Geophysical Research: Atmospheres*, *119*, 9359–9375. <https://doi.org/10.1002/2014JD021833>

- Fritts, D. C., Dong, W., Lund, T. S., & Laughman, B. (2020). Self-acceleration and instability of gravity wave packets: 3. Three-dimensional packet propagation, secondary gravity waves, momentum transport, and transient mean forcing in tidal winds. *Journal of Geophysical Research: Atmospheres*, *125*, e2019JD030692. <https://doi.org/10.1029/2019JD030692>
- Fritts, D. C., Laughman, B., Wang, L., Lund, T., & Collins, R. L. (2018). Gravity wave dynamics in a mesospheric inversion layer: 1. Reflection, trapping, and instability dynamics. *Journal of Geophysical Research: Atmospheres*, *123*, 626–648. <https://doi.org/10.1002/2017JD027440>
- Fritts, D. C., Miller, A. D., Kjellstrand, C. B., Geach, C., Williams, B. P., Kaifler, B., et al. (2019). PMC Turbo: Studying gravity wave and instability dynamics in the summer mesosphere using polar mesospheric cloud imaging and profiling from a stratospheric balloon. *Journal of Geophysical Research: Atmospheres*, *124*, 6423–6443. <https://doi.org/10.1029/2019JD030298>
- Fritts, D. C., Wang, L., Baumgarten, G., Miller, A. D., Geller, M. A., Jones, G., et al. (2017). High-resolution observations and Modeling of turbulence sources, structures, and intensities in the upper mesosphere. *Journal of Atmospheric and Solar - Terrestrial Physics*, *162*, 57–78. <https://doi.org/10.1016/j.jastp.2016.11.006>
- Fritts, D. C., Wang, L., Laughman, B., Lund, T., & Collins, R. L. (2018). Gravity wave dynamics in a mesospheric inversion layer: 2. Instabilities, turbulence, fluxes, and mixing. *Journal of Geophysical Research: Atmospheres*, *123*, 649–670. <https://doi.org/10.1002/2017JD027442>
- Fritts, D. C., Wang, L., Taylor, M. J., Pautet, P.-D., Criddle, N. R., Kaifler, B., et al. (2019). Large-amplitude mountain waves in the mesosphere observed on 21 June 2014 during DEEPWAVE: 2. Nonlinear dynamics, wave breaking, and instabilities. *Journal of Geophysical Research: Atmospheres*, *124*, 10,006–10,032. <https://doi.org/10.1029/2019JD030899>
- Fritts, D. C., Wang, L., Werne, J., Lund, T., & Wan, K. (2009). Gravity wave instability dynamics at high Reynolds numbers, 1: Wave field evolution at large amplitudes and high frequencies. *Journal of the Atmospheric Sciences*, *66*, 1126–1148. <https://doi.org/10.1175/2008JAS2726.1>
- Fritts, D. C., & Yuan, L. (1989). An analysis of gravity wave ducting in the atmosphere: Eckart's resonances in thermal and Doppler ducts. *Journal of Geophysical Research*, *94*, 18,455–18,466.
- Gadsden, M., & Schröder, W. (1989). *Noctilucent Clouds*. Berlin: Springer-Verlag.
- Giongo, G. A., Bageston, J. V., Batista, P. P., Wrasse, C. M., Bittencourt, G. D., Paulino, I., et al. (2018). Mesospheric front observations by the OH airglow imager carried out at Ferraz Station on King George Island, Antarctic peninsula, in 2011. *Annales de Geophysique*, *36*, 253–264. <https://doi.org/10.5194/angeo-36-253-2018>
- Grimshaw, R. (1981a). Evolution equations for long nonlinear internal waves in stratified shear flows. *Studies in Applied Mathematics*, *65*, 159–188.
- Grimshaw, R. (1981b). Solitary waves in a compressible fluid. *Pure and Applied Geophysics*, *119*(4), 780–797. <https://doi.org/10.1007/BF01131255>
- Grimshaw, R. (1981c). A second-order theory for solitary waves in deep fluids. *Physics of Fluids*, *24*, 1611–1618. <https://doi.org/10.1063/1.863583>
- Grimshaw, R., Broutman, D., Laughman, B., & Eckermann, S. D. (2015). Solitary waves and undular bores in a mesosphere duct. *Journal of the Atmospheric Sciences*, *72*, 4412–4422. <https://doi.org/10.1175/JAS-D-14-0351.1>
- Grimshaw, R. H. J. (2002). Internal solitary waves. In R. Grimshaw (Ed.), *Environmental Stratified Flows, Topics Environ. Fluid Mechanics, Vol. 3*, (pp. 1–29). Dordrecht, Netherlands: Kluwer Acad.
- Hervig, M. E., Gordley, L. L., Stevens, M., Russell, J. M., & Bailey, S. (2009). Interpretation of SOFIE PMC measurements: Cloud identification and derivation of mass density, particle shape, and particle size. *Journal of Atmospheric and Solar - Terrestrial Physics*, *71*. <https://doi.org/10.1016/j.jastp.2008.07.009>
- Kaifler, B., Kaifler, N., Ehard, B., Drnbrack, A., Rapp, M., & Fritts, D. C. (2015). Influences of source conditions on mountain wave penetration into the stratosphere and mesosphere. *Geophysical Research Letters*, *42*, 9488–9494. <https://doi.org/10.1002/2015GL066465>
- Lamb, H. (1932). *Hydrodynamics*, (6th ed.). New York: Cambridge Univ. Press.
- Laughman, B., Fritts, D. C., & Werne, J. (2009). Numerical simulation of bore generation and morphology in thermal and Doppler ducts. *Annales de Geophysique*, *27*, 511–523. <https://doi.org/10.5194/angeo-27-511-2009>
- Laughman, B., Fritts, D. C., & Werne, J. (2011). Comparisons of predicted bore evolutions by the Benjamin–Davis–Ono and Navier–Stokes equations for idealized mesopause thermal ducts. *Journal of Geophysical Research*, *116*, D02120. <https://doi.org/10.1029/2010JD014409>
- Li, F., Swenson, G. R., Liu, A. Z., Taylor, M., & Zhao, Y. (2007). Investigation of a “wall” wave event. *Journal of Geophysical Research*, *112*, D04104. <https://doi.org/10.1029/2006JD007213>
- Li, Q., Xu, J., Yue, J., Liu, X., Yuan, W., Ning, B., et al. (2013). Investigation of a mesospheric bore event over northern China. *Annales de Geophysique*, *31*, 409–418. <https://doi.org/10.5194/angeo-31-409-2013>
- Lighthill, J. (1979). *Waves in Fluids*, 504 Pp. Cambridge, U. K: Cambridge Univ. Press.
- Medeiros, A., Fechine, J., Buriti, R. A., Takahashi, H., Wrasse, C. M., & Gobbi, D. (2005). Response of OH, O₂ and OI5577 airglow emissions to the mesospheric bore in the equatorial region of Brazil. *Advances in Space Research*, *35*, 1971–1975. <https://doi.org/10.1016/j.asr.2005.03.075>
- Medeiros, A. F., Paulino, I., Taylor, M. J., Fechine, J., Takahashi, H., Buriti, R. A., et al. (2016). Twin mesospheric bores observed over Brazilian equatorial region. *Annales de Geophysique*, *34*, 91–96. <https://doi.org/10.5194/angeo-34-91-2016>
- Medeiros, A. F., Paulino, I., Wrasse, C. M., Fechine, J., Takahashi, H., Bageston, J. V., et al. (2018). Case study of mesospheric front dissipation observed over the northeast of Brazil. *Annales de Geophysique*, *36*, 311–319. <https://doi.org/10.5194/angeo-36-311>
- Medeiros, A. F., Taylor, M. J., Takahashi, H., Batista, P. P., & Gobbi, D. (2001). An unusual airglow wave event observed at Cachoeira Paulista 23°S. *Advances in Space Research*, *27*(10), 1749–1754. [https://doi.org/10.1016/S0273-1177\(01\)00317-9](https://doi.org/10.1016/S0273-1177(01)00317-9)
- Miller, A. D., Fritts, D. C., Chapman, D., Jones, G., Limon, M., Araujo, D., et al. (2015). Stratospheric imaging of polar mesospheric clouds: A new window on small-scale atmospheric dynamics. *Geophysical Research Letters*, *42*, 6058–6065. <https://doi.org/10.1002/2015GL064758>
- Narayanan, V. L., Gurubaran, S., & Emperumal, K. (2009). A case study of a mesospheric bore event observed with an all-sky airglow imager at Tirunelveli (8.7°N). *Journal of Geophysical Research*, *114*, D08114. <https://doi.org/10.1029/2008JD010602>
- Narayanan, V. L., Gurubaran, S., & Emperumal, K. (2012). Nightglow imaging of different types of events, including a mesospheric bore observed on the night of February 15, 2007 from Tirunelveli (8.7°N). *Journal of Atmospheric and Solar - Terrestrial Physics*, *78–79*, 70–83. <https://doi.org/10.1016/j.jastp.2011.07.006>
- Nielsen, K., Taylor, M. J., Stockwell, R. G., & Jarvis, M. J. (2006). An unusual mesospheric bore event observed at high latitudes over Antarctica. *Geophysical Research Letters*, *33*, L07803. <https://doi.org/10.1029/2005GL025649>

- Rapp, M., Strelnikov, B., Mullemann, A., Luebken, F.-J., & Fritts, D. C. (2004). Turbulence measurements and implications for gravity wave dissipation during the MaCWAVE/MIDAS rocket program. *Geophysical Research Letters*, *31*, L24S07. <https://doi.org/10.1029/2003GL019325>
- Rapp, M., & Thomas, G. E. (2006). Modeling the microphysics of mesospheric ice particles: Assessment of current capabilities and basic sensitivities. *Journal of Atmospheric and Solar - Terrestrial Physics*, *68*, 715–744.
- Rayleigh, L. (1908). Note on tidal bores, Proc. R. Soc. London, Ser. A, 81, 448–449. (Reprinted in Scientific Papers by Lord Rayleigh, vol. 5, Pap. 333, p. 495, Dover, Mineola, N. Y., 1964.)
- Rottman, J. W., & Einaudi, F. (1993). Solitary waves in the atmosphere. *Journal of the Atmospheric Sciences*, *50*, 2116–2136. [https://doi.org/10.1175/1520-0469\(1993\)050%3C2116:SWITA%3E2.0.CO;2](https://doi.org/10.1175/1520-0469(1993)050%3C2116:SWITA%3E2.0.CO;2)
- Rottman, J. W., & Grimshaw, R. (2003). Atmospheric Internal Solitary Waves. R. Grimshaw *Environmental Stratified Flows. Topics in Environmental Fluid Mechanics* (Vol. 3, pp. 61–88). Boston, MA: Springer. https://doi.org/10.1007/0-306-48024-7_3
- She, C. Y., Li, T., Williams, B. P., & Yuan, T. (2004). Concurrent OH imager and sodium temperature/wind lidar observation of a mesopause region undular bore event over Fort Collins/Platteville, Colorado. *Journal of Geophysical Research*, *109*, D22107. <https://doi.org/10.1029/2004JD004742>
- Shiokawa, K., Suzuki, S., Otsuka, Y., Ogawa, T., Nakamura, T., Mlynarczyk, M. G., & Russell, M. J. (2006). A multi-instrument measurement of a mesospheric front-like structure at the equator. *Journal of the Meteorological Society of Japan*, *84A*, 305–316. <https://doi.org/10.2151/jmsj.84A.305>
- Smith, R. K. (1988). Traveling waves and bores in the lower atmosphere: The “morning glory” and related phenomena. *Earth Science Reviews*, *25*, 267–290. [https://doi.org/10.1016/0012-8252\(88\)90069-4](https://doi.org/10.1016/0012-8252(88)90069-4)
- Smith, S. M. (2014). The identification of mesospheric frontal gravity wave events at a mid-latitude site. *Advances in Space Research*, *54*, 417–424. <https://doi.org/10.1016/j.asr.2013.08.014>
- Smith, S. M., Friedman, J., Raizada, S., Tepley, C., Baumgardner, J., & Mendillo, M. (2005). Evidence of mesospheric bore formation from a breaking gravity wave event: Simultaneous imaging and lidar measurements. *Journal of Atmospheric and Solar - Terrestrial Physics*, *67*, 345–356. <https://doi.org/10.1016/j.jastp.2004.11.008>
- Smith, S. M., Sheer, J., Raizada, S., Reisin, E., Baumgardner, J., & Mendillo, M. (2006). Characterization of exceptionally strong mesospheric wave event using all-sky and zenith airglow observations. *Journal of Geophysical Research*, *111*, A09309. <https://doi.org/10.1029/2005JA011197>
- Smith, S. M., Stober, G., Jacobi, C., Chau, J. L., Gerding, M., Baumgardner, J. L., et al. (2017). Characterization of a double mesospheric bore over Europe. *Journal of Geophysical Research*, *122*, 9738–9750. <https://doi.org/10.1002/2017JA024225>
- Smith, S. M., Taylor, M. J., Swenson, G. R., She, C.-Y., Hocking, W., Baumgardner, J., & Mendillo, M. (2003). A multidagnostic investigation of the mesospheric bore phenomenon. *Journal of Geophysical Research*, *108*(A2), 1083. <https://doi.org/10.1029/2002JA009500>
- Snively, J., & Pasko, V. P. (2003). Breaking of thunderstorm generated gravity waves as a source of short-period ducted waves at mesopause altitudes. *Geophysical Research Letters*, *30*(24), 2254. <https://doi.org/10.1029/2003GL018436>
- Snively, J. B., & Pasko, V. P. (2008). Excitation of ducted gravity waves in the lower thermosphere by tropospheric sources. *Journal of Geophysical Research*, *113*, A06303. <https://doi.org/10.1029/2007JA012693>
- Stockwell, R. G., Taylor, M. J., Nielsen, K., & Jarvis, M. A. (2006). A novel joint space-wavenumber analysis of an unusual Antarctic gravity wave event. *Geophysical Research Letters*, *33*, L08805. <https://doi.org/10.1029/2005GL025660>
- Stockwell, R. G., Taylor, M. J., Nielsen, K. K., & Jarvis, M. J. (2011). The evolution of a breaking mesospheric bore wave packet. *Journal of Geophysical Research*, *116*, D19102. <https://doi.org/10.1029/2010JD015321>
- Swenson, G. R., & Epsy, P. J. (1995). Observations of 2-dimensional airglow structure and Na density from the ALOHA, October 9, 1993 ‘storm flight’. *Geophysical Research Letters*, *22*(20), 2845–2848. <https://doi.org/10.1029/95GL02795>
- Swenson, G. R., Qian, J., Plane, J. M. C., Epsy, P. J., Taylor, M. J., Turnbull, D. N., & Lowe, R. P. (1998). Dynamical and chemical aspects of the mesospheric Na “wall” event on October 9, 1993 during the airborne lidar and observations of Hawaiian airglow (ALOHA) campaign. *Journal of Geophysical Research*, *103*, 6361–6380. <https://doi.org/10.1029/97JD03379>
- Taylor, M. J., Turnbull, D. N., & Lowe, R. P. (1995). Spectrometric and imaging measurements of a spectacular gravity wave event observed during the ALOHA-93 campaign. *Geophysical Research Letters*, *22*, 2849–2852. <https://doi.org/10.1029/95GL02948>
- Thayer, J. P., Nielsen, N., & Jacobsen, J. (1995). Noctilucent cloud observations over Greenland by a Rayleigh lidar. *Geophysical Research Letters*, *22*(21). <https://doi.org/10.1029/95GL02126>
- Tricker, R. A. R. (1965). *Bores, Breakers, Waves, and Wakes*. New York: Elsevier.
- Walterscheid, R. L., Hecht, J. H., Gelin, L. J., Hickey, M. P., & Reid, I. M. (2012). An intense traveling airglow front in the upper mesosphere–lower thermosphere with characteristics of a bore observed over Alice Springs, Australia, during a strong 2 day wave episode. *Journal of Geophysical Research*, *117*, D22105. <https://doi.org/10.1029/2012JD017847>
- Walterscheid, R. L., Schubert, G., & Brinkman, D. G. (2001). Small-scale gravity waves in the upper mesosphere and lower thermosphere generated by deep tropical convection. *Journal of Geophysical Research*, *106*(D23), 31,825–31,832.
- Yue, J., She, C.-Y., Nakamura, T., Harrell, S., & Yuan, T. (2010). Mesospheric bore formation from large-scale gravity wave perturbations observed by collocated all-sky OH imager and sodium lidar. *Journal of Atmospheric and Solar - Terrestrial Physics*, *72*(1), 7–18. <https://doi.org/10.1016/j.jastp.2009.10.002>